Journal of Low Temperature Physics, Vol. 129, Nos. 5/6, December 2002 (© 2002)

Bose-Einstein Condensates in Dilute Trapped Atomic Gases

Alexander L. Fetter

Department of Physics and Geballe Laboratory for Advanced Materials, Stanford University, Stanford, California 94305-4045, USA

The static and dynamic behavior of dilute trapped Bose-Einstein condensates at low temperature follows from the Gross-Pitaevskii equation for the condensate and the Bogoliubov equations for the linearized small-amplitude normal modes. The uniform system serves to illustrate the theoretical methods and much of the basic physics. The principal new effect of the confining trap is to introduce an additional length scale (the size of the single-particle ground state) and energy scale (the single-particle ground-state energy). Most recent experiments use large condensates, when the repulsive interactions expand the condensate considerably and thus reduce the kinetic energy associated with the nonuniform density. In this regime (known as the "Thomas-Fermi" limit), the system can be treated as locally uniform, which greatly simplifies the analysis. When the condensate contains one or more vortex lines, the nonuniform trap potential and local line curvature drive the resulting vortex motion. Experiments have confirmed various predicted precessional motions in considerable detail. Mixtures of two distinct bosonic species allow for new coupled dynamical motions that alter the topology of the original single complex order parameter. In particular, application of near-resonant electromagnetic fields yields a coupled system that no longer has quantized circulation. Such experimental techniques created the first vortex line by spinning up one of the components. The introduction of optical traps has allowed the study of what are called "spinor" condensates. In this case, all hyperfine states are trapped, in contrast to the more common magnetic traps that confine only a subset of the various hyperfine states. The rotational invariance of the interparticle interactions significantly restricts the allowed states of these spinor condensates.

PACS numbers: 03.75.Fi, 67.40.Vs, 47.37.+q

0022-2291/02/1200-0263/0

1. BASIC PHYSICS OF BOSE-EINSTEIN CONDENSATION IN A TRAP

These notes make no attempt to provide comprehensive references; good recent accounts can be found in Refs. 1-3. Consider an ideal uniform gas of N identical particles confined in a volume $V = L^3$ with mean density $n = N/V$ (see, for example, Refs. 4,5). At temperature T, the mean kinetic energy per particle $p^2/2M \sim k_B T$ implies a thermal De Broglie wavelength $\lambda_T = (2\pi\hbar^2/Mk_BT)^{1/2} \sim h/p$ associated with the quantum-mechanical matter waves in thermal equilibrium. At high temperature (or in the classical limit, $\hbar \to 0$), λ_T is small compared to the interparticle spacing $l \sim n^{-1/3}$. In this short-wavelength limit, the particles follow definite trajectories, analogous to light rays in geometric optics. As the temperature falls, however, λ_T eventually becomes comparable with the interparticle spacing. When $n\lambda_T^3 \sim 1$, quantum degeneracy becomes important. Equivalently, k_BT becomes comparable with the zero-point energy $\hbar^2 n^{2/3}/M$ associated with confinement in a box of volume n^{-1} (the only energy that can be formed from the interparticle spacing). For fermions, this yields the Fermi temperature T_F when the Pauli exclusion principle starts to play a significant role. For bosons, the same temperature characterizes the onset of Bose-Einstein condensation (BEC), when a macroscopic number of particles starts to occupy the lowest single-particle state. For liquid helium at its equilibrium density, this temperature is $\sim$ 1 K for both isotopes (^{3}He is a fermion and ^{4}He is a boson). The corresponding temperatures for dilute atomic gases are $\sim$ 100 - 1000 nK because of the much lower density and higher atomic mass.

1.1. Ideal Bose Gas

Consider an ideal Bose gas confined in an external potential $V_{\rm ex}$. The single-particle states ψ_j and eigenvalues ϵ_j obey the Schrödinger equation

$$(T + V_{\rm ex})\,\psi_j = \epsilon_j \psi_j, \tag{1}$$

where $T = -\hbar^2\nabla^2/2M$ is the kinetic-energy operator. It is convenient to use the grand canonical ensemble, where the system is in equilibrium with a particle reservoir at chemical potential μ, so that the number of particles can fluctuate (eventually, we express the chemical potential in terms of the particle number N). The mean occupation of the jth state is

$$n_j = \frac{1}{\exp[\beta(\epsilon_j - \mu)] - 1} \equiv f(\epsilon_j), \tag{2}$$

where $\beta = 1/k_B T$ is the inverse temperature and $f(\epsilon) = \{\exp[\beta(\epsilon-\mu)]-1\}^{-1}$ is the familiar Bose-Einstein distribution function. Correspondingly, the mean number of particles and mean energy are

$$N = \sum_j f(\epsilon_j) \equiv N(T,\mu), \tag{3}$$

$$E = \sum_j \epsilon_j f(\epsilon_j) \equiv E(T,\mu). \tag{4}$$

Equation (3) expresses the mean number in terms of the temperature and chemical potential, and it can be inverted (at least formally) to determine the chemical potential $\mu(T,N)$ for given T and N. Substitution into Eq. (4) then gives $E(T,N)$.

In the high-temperature (or classical) limit, the chemical potential $\mu(T,N)$ is large and negative, and the distribution function reduces to the Maxwell-Boltzmann form $f(\epsilon) \approx e^{\beta(\mu-\epsilon)}$. As the temperature falls, however, μ increases, and the occupation n_0 of the lowest single-particle state becomes singular at a critical temperature T_c defined by $\mu(T_c,N) = \epsilon_0$. This behavior signals the onset of Bose-Einstein condensation.

It is useful to introduce the density of states

$$g(\epsilon) \equiv \sum_j \delta(\epsilon - \epsilon_j), \tag{5}$$

in which case Eqs. (3) and (4) take simple forms

$$N = \int d\epsilon\, g(\epsilon) f(\epsilon), \tag{6}$$

$$E = \int d\epsilon\, \epsilon\, g(\epsilon) f(\epsilon). \tag{7}$$

For $T < T_c$, the chemical potential remains fixed at $\mu(T_c,N) = \epsilon_0$, and the ground state has a macroscopic occupation $N_0(T)$ whose temperature dependence is determined by

$$N = N_0(T) + N'(T), \quad \text{with} \quad N'(T) = \int_{\epsilon_0}^{\infty} d\epsilon\, \frac{g(\epsilon)}{\exp[\beta(\epsilon-\epsilon_0)]-1}. \tag{8}$$

1.1.1. BEC in a box with periodic boundary conditions

The simplest example is a box of volume V, when the eigenfunctions are plane waves $\psi_{\mathbf{k}}(\mathbf{r}) = V^{-1/2}\exp(i\mathbf{k}\cdot\mathbf{r})$, with the energy $\epsilon_k = \hbar^2 k^2/2M$. In the thermodynamic limit $N \to \infty$, $V \to \infty$, the density of states is

$$g(\epsilon) \approx \frac{V}{8\pi^3} \int d^3k\, \delta\left(\epsilon - \frac{\hbar^2 k^2}{2M}\right) = \frac{V}{4\pi^2}\left(\frac{2M}{\hbar^2}\right)^{3/2} \sqrt{\epsilon}. \tag{9}$$

Since $\epsilon_0 = 0$, the onset of Bose-Einstein condensation occurs at $\mu(T_c, N) = 0$, with

$$N = \frac{V}{4\pi^2}\left(\frac{2M}{\hbar^2}\right)^{3/2} \int_0^\infty d\epsilon \, \frac{\sqrt{\epsilon}}{\exp(\beta_c \epsilon) - 1}. \tag{10}$$

The integral is readily evaluated, and the onset of quantum degeneracy occurs at

$$n\lambda_{T_c}^3 = \zeta(\tfrac{3}{2}) \approx 2.612, \tag{11}$$

which is the critical phase-space density for onset of BEC in a box, as anticipated from the qualitative arguments given above. Equivalently, the onset Bose-condensation temperature for an ideal Bose gas with number density n is

$$k_B T_c \approx 3.31 \, \frac{\hbar^2 n^{2/3}}{M}. \tag{12}$$

For $T < T_c$, the chemical potential remains zero in the thermodynamic limit of large N and V, with a discontinuous second derivative at T_c, indicating the presence of a true phase transition. For an ideal Bose gas in a box, Eq. (8) yields

$$\frac{N_0(T)}{N} = 1 - \left(\frac{T}{T_c}\right)^{3/2}. \tag{13}$$

Note that $N_0(0) = N$, so that the ground-state occupation is complete at zero temperature.

1.1.2. BEC in a harmonic trapping potential

Formally, the experimentally interesting case of BEC for an ideal Bose gas in a harmonic trap differs only in the detailed form of the single-particle energy spectrum and the associated density of states. For a trap potential $V_{\rm tr}(\mathbf{r}) = \frac{1}{2}M\left(\omega_x^2 x^2 + \omega_y^2 y^2 + \omega_z^2 z^2\right)$, the energy levels are (we omit the zero-point energy that simply shifts the chemical potential)

$$\epsilon_{n_x n_y n_z} = \hbar\left(n_x\omega_x + n_y\omega_y + n_z\omega_z\right), \tag{14}$$

labeled by a triplet of non-negative integers n_x, n_y, n_z. The density of states is

$$g(\epsilon) = \sum_{n_x,n_y,n_z=0}^{\infty} \delta\left(\epsilon - \epsilon_{n_x n_y n_z}\right). \tag{15}$$

For small ϵ, only a few states contribute, and the resulting density of states has a step-like structure. For large ϵ, many states contribute and the sum can be approximated by an integral

$$g(\epsilon) \approx \frac{1}{\hbar^3\omega_0^3} \int_0^\infty du\, dv\, dw\, \delta(\epsilon - u - v - w) = \frac{\epsilon^2}{2\hbar^3\omega_0^3}, \tag{16}$$

where $\omega_0 = (\omega_x\omega_y\omega_z)^{1/3}$ is the geometric mean of the trap frequencies.

With our definitions, the onset of BEC in a harmonic trap occurs at $\mu = 0$, and a straightforward calculation shows that

$$k_B T_c = \left(\frac{1}{\zeta(3)}\right)^{1/3} \hbar\omega_0\, N^{1/3} \approx 0.94\, \hbar\omega_0\, N^{1/3} \tag{17}$$

for onset of BEC in a harmonic trap, where $\zeta(3) \approx 1.202$. For $T < T_c$, the macroscopic occupation of the ground state has the temperature dependence

$$\frac{N_0(T)}{N} = 1 - \left(\frac{T}{T_c}\right)^3, \tag{18}$$

again showing that the ground state of an ideal Bose gas is fully occupied at $T = 0$ K. This ground state has a gaussian density distribution with a mean width $d_0 = \sqrt{\hbar/M\omega_0}$. In contrast, the classical density profile in the same potential $V_{\rm tr}$ is given by $n(\mathbf{r}) \propto \exp[-\beta V_{\rm tr}(\mathbf{r})]$. For a spherical potential, this density represents an isotropic gaussian distribution with a characteristic thermal width $R_T = \sqrt{2k_BT/M\omega_0^2}$ that is the classical turning point for a particle with energy k_BT. Typical traps have $d_0 \sim$ a few μm and $N \sim 10^6$. At the transition temperature, the ratio of the thermal width to the ground-state width is $R_{T_c}/d_0 \sim N^{1/6} \sim 10$, so that the onset of BEC in a trap leads to a dramatic narrow ground-state peak that rises out of the much wider diffuse thermal cloud[6] (see Fig. 1). In addition, since $k_BT_c/\hbar\omega_0 \sim N^{1/3} \sim 100$, the classical picture of the thermal cloud remains valid even at T_c. The mean density at the transition is $n_c \sim N/R_{T_c}^3$, typically much smaller than the corresponding ground-state value $n_0 \sim N/d_0^3$.

In contrast to a uniform ideal Bose gas in a box, the case of BEC in a given trap does not strictly have a thermodynamic limit, because the density can remain constant only if the trap parameters vary in an appropriate way as $N \to \infty$. This also means that there is strictly no sharp phase transition,

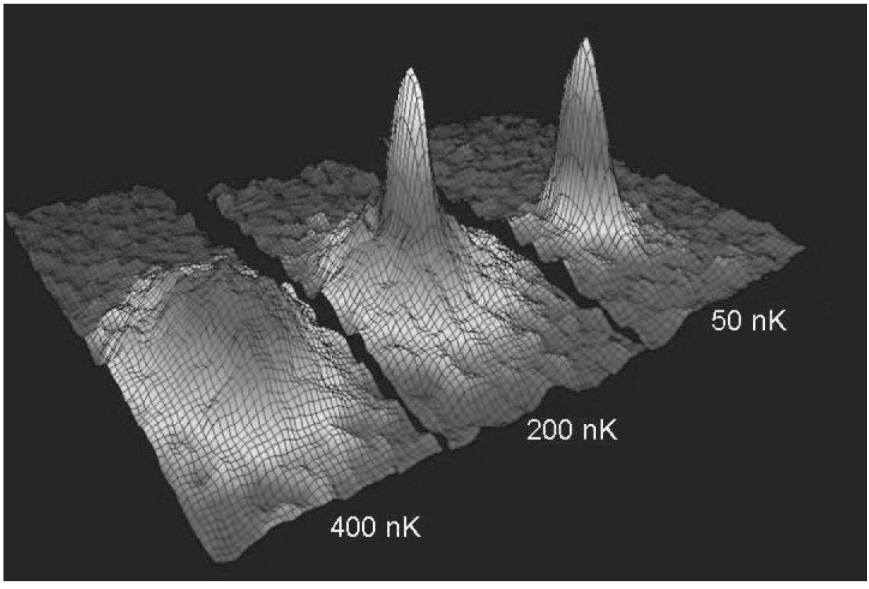

Fig. 1. Images of velocity distribution in experiment by Anderson *et al.*[6] (1995). Left frame corresponds to gas at temperature just above condensation; center frame, just after appearance of condensate; right frame, after further evaporation leaves nearly pure condensate [from J. Res. NIST 101(4) (1996)].

but detailed numerical studies show that the resulting rounding near T_c generally becomes unobservable for typical experimental parameters.

1.2. Inclusion of Interparticle Interactions

Bogoliubov's original paper on the uniform weakly interacting Bose gas[7] focused clearly on the crucial role of the Bose-Einstein condensate in determining the ground state and low-lying excited states of a dilute interacting Bose gas at zero temperature. For low density n and short-range interactions characterized by an s-wave scattering length a, the small gas parameter $na^3 \ll 1$ provides a suitable basis for an expansion relative to the behavior of the ideal Bose gas (equivalently, the scattering length a is small compared to the interparticle separation $n^{-1/3}$). In this limit, the true interacting ground state is assumed to be "close" to that of an ideal Bose gas, in that the occupation N_0 of the single-particle ground state remains comparable to the total number of particles, with $N_0 \lesssim N$.

1.2.1. *Bogoliubov approximation for a uniform Bose gas*

In the dilute limit, only s-wave two-body scattering is important, and the interparticle potential can be approximated by a short-range "pseudopotential" $V(\mathbf{r}) \approx g\delta(\mathbf{r})$. Standard scattering theory shows that the s-wave scattering length a fixes the interaction strength through the relation $g \approx 4\pi a\hbar^2/M$.[8] For such a potential, the second-quantized Hamiltonian for the interacting system in a box of volume V takes the form

$$\hat{H} = \sum_{\mathbf{k}} \epsilon_k \, a^\dagger_{\mathbf{k}} a_{\mathbf{k}} + \frac{g}{2V} \sum_{\mathbf{k}_1\mathbf{k}_2\mathbf{k}_3\mathbf{k}_4} a^\dagger_{\mathbf{k}_1} a^\dagger_{\mathbf{k}_2} a_{\mathbf{k}_3} a_{\mathbf{k}_4} \, \delta_{\mathbf{k}_1+\mathbf{k}_2,\mathbf{k}_3+\mathbf{k}_4}, \tag{19}$$

where the operators obey the usual Bose-Einstein commutation relations $[a_{\mathbf{k}}, a^\dagger_{\mathbf{k}'}] = \delta_{\mathbf{k}\mathbf{k}'}$, $[a^\dagger_{\mathbf{k}}, a^\dagger_{\mathbf{k}'}] = [a_{\mathbf{k}}, a_{\mathbf{k}'}] = 0$. The basic assumption is that the operators a_0 and $a^\dagger_0$ associated with the single-particle ground state are of order $\sqrt{N_0}$, whereas their commutator is unity. Hence, they can be treated as classical fields to leading order, merely making the replacements $a_0, a^\dagger_0 \to \sqrt{N_0}$ in the Hamiltonian, Eq. (19). In this way, the many-body Hamiltonian becomes a quadratic form[8]

$$\hat{H} = \frac{gN_0^2}{2V} + \sum_{\mathbf{k}\neq 0} \left(\epsilon_k + \frac{2gN_0}{V}\right) a^\dagger_{\mathbf{k}} a_{\mathbf{k}} + \frac{gN_0}{2V} \sum_{\mathbf{k}\neq 0} \left(a^\dagger_{\mathbf{k}} a^\dagger_{-\mathbf{k}} + a_{\mathbf{k}} a_{-\mathbf{k}}\right). \tag{20}$$

Note the unusual structure containing terms that do not conserve particle number. Consequently, it is convenient to consider only states with a fixed number N of particles, so that the number operator

$$\hat{N} = N_0 + \sum_{\mathbf{k}\neq 0} a^\dagger_{\mathbf{k}} a_{\mathbf{k}} \tag{21}$$

can then be replaced by its eigenvalue N. Equation (21) can be used to eliminate N_0 in favor of N through terms of order N^2 and N. As a result, the model Hamiltonian, Eq. (20), becomes

$$\hat{H} = \frac{gN^2}{2V} + \sum_{\mathbf{k}\neq 0} (\epsilon_k + gn) \, a^\dagger_{\mathbf{k}} a_{\mathbf{k}} + \frac{gn}{2} \sum_{\mathbf{k}\neq 0} \left(a^\dagger_{\mathbf{k}} a^\dagger_{-\mathbf{k}} + a_{\mathbf{k}} a_{-\mathbf{k}}\right). \tag{22}$$

The operator part of Eq. (22) can be diagonalized by a linear canonical transformation

$$a_{\mathbf{k}} = u_k \alpha_{\mathbf{k}} - v_k \alpha^\dagger_{-\mathbf{k}}, \quad a^\dagger_{-\mathbf{k}} = u_k \alpha^\dagger_{-\mathbf{k}} - v_k \alpha_{\mathbf{k}} \tag{23}$$

to new quasiparticle operators $\alpha_{\mathbf{k}}$ and $\alpha_{\mathbf{k}}^\dagger$ that obey the same Bose commutation relations $[\alpha_{\mathbf{k}}, \alpha_{\mathbf{k}'}^\dagger] = \delta_{\mathbf{k}\mathbf{k}'}$, $[\alpha_{\mathbf{k}}^\dagger, \alpha_{\mathbf{k}'}^\dagger] = [\alpha_{\mathbf{k}}, \alpha_{\mathbf{k}'}] = 0$. This condition requires that $u_k^2 - v_k^2 = 1$ for all $\mathbf{k} \neq 0$. A detailed analysis shows that the relevant part of the Hamiltonian reduces to a set of uncoupled harmonic oscillators with

$$\hat{H} \approx \text{const} + \sum_{\mathbf{k}\neq 0} E_k \, \alpha_{\mathbf{k}}^\dagger \alpha_{\mathbf{k}}. \tag{24}$$

Here the energy associated with the quasiparticle normal mode $\mathbf{k}$ is

$$E_k = \sqrt{(\epsilon_k + gn)^2 - (gn)^2} = \sqrt{\epsilon_k^2 + 2\epsilon_k gn} \tag{25}$$

along with the transformation parameters

$$v_k^2 = u_k^2 - 1 = \frac{1}{2}\left(\frac{\epsilon_k + gn}{E_k} - 1\right). \tag{26}$$

The condition that E_k be real for all $\mathbf{k}$ requires a repulsive interaction with $a > 0$ (the situation is different for a trapped condensate).

The quasiparticle Hamiltonian, Eq. (24), implies a very simple structure for the ground state and the excited states in the Bogoliubov approximation. Since $\alpha_{\mathbf{k}}^\dagger \alpha_{\mathbf{k}}$ has the eigenvalues $0, 1, 2, \ldots$, the ground-state $|\Phi\rangle$ of this model Hamiltonian is the quasiparticle vacuum defined by

$$\alpha_{\mathbf{k}}|\Phi\rangle = 0 \quad \text{for all } \mathbf{k} \neq 0; \tag{27}$$

evidently, $|\Phi\rangle$ is a very complicated combination of unperturbed single-particle states, for neither $a_{\mathbf{k}}$ nor $a_{\mathbf{k}}^\dagger$ annihilates it. Correspondingly, the excited states are obtained by applying various quasiparticle creation operators $\alpha_{\mathbf{k}}^\dagger$ to $|\Phi\rangle$.

More generally, the quasiparticle Hamiltonian for a dilute Bose gas at low temperature typically has a structure $\hat{H} = \text{const} + \sum_j \hbar\omega_j \alpha_j^\dagger \alpha_j$ similar to Eq. (24), but with j now denoting a complete set of self-consistent single-particle states. The corresponding normal-mode excitation frequencies ω_j often depend on various parameters. Since the quasiparticle number operator $\alpha_j^\dagger \alpha_j$ necessarily has non-negative eigenvalues, the system is unstable if any one of the eigenvalues ω_j becomes negative. An example of such behavior is considered below in connection with the Landau critical velocity for a uniform condensate moving with velocity $\mathbf{v}$, and similar ideas are crucial in understanding the stability of a vortex line in a rotating Bose condensate.

The physics of the quasiparticles is very transparent, for the excitation energy associated with a quasiparticle of wave vector $\mathbf{k}$ is [compare with Eq. (25)]

$$E_k \approx \begin{cases} \sqrt{\frac{ng}{M}}\,\hbar k = \sqrt{\frac{4\pi a\hbar^2 n}{M^2}}\,\hbar k, & \text{for } k \to 0; \\ \epsilon_k + \frac{4\pi a\hbar^2 n}{M}, & \text{for } k \to \infty. \end{cases} \tag{28}$$

In the long-wavelength limit, the elementary excitations represent sound waves with the propagation speed

$$s = \sqrt{\frac{ng}{M}} = \frac{\hbar}{M}\sqrt{4\pi a n}, \tag{29}$$

which again shows that g and a must be positive for a uniform Bose gas. For short wavelengths, the spectrum is that of a free particle shifted upward by the "Hartree" interaction $V_H = 4\pi a\hbar^2 n/M = gn$ with the background particles. The crossover between the two regimes occurs when $\epsilon_k \approx ng = 4\pi a\hbar^2 n/M$, which leads the characteristic length

$$\xi = \frac{1}{\sqrt{8\pi n a}}, \tag{30}$$

known as the "healing length" (or correlation length or coherence length). Since $\xi \to \infty$ as $a \to 0$, the crossover at $k \approx 1/\xi$ then moves to zero, reproducing the quadratic spectrum of the ideal Bose gas in a box.

The Bogoliubov transformation, Eq. (23), can be easily inverted to yield

$$\alpha_{\mathbf{k}} = u_k a_{\mathbf{k}} + v_k a^\dagger_{-\mathbf{k}}, \quad \alpha^\dagger_{-\mathbf{k}} = u_k a^\dagger_{-\mathbf{k}} + v_k a_{\mathbf{k}}. \tag{31}$$

The quasiparticle operators are linear superpositions of particle and hole operators, with u_k and v_k as weight factors. In the phonon regime ($k\xi \ll 1$), each coefficient is large ($u_k^2 \approx v_k^2 \propto 1/k\xi$), so that the quasiparticle operators are coherent nearly equal admixtures. In the free-particle regime, however, $u_k^2 \approx 1$ and $v_k^2 \propto (k\xi)^{-4}$, leading to effectively pure particle operators.

As an example of the power of these methods, we consider the ground-state depletion of the zero-momentum state caused by the repulsive interactions $N'(0)/N = 1 - N_0(0)/N$. The ground-state expectation value of Eq. (21), $\langle\Phi|\hat{N}|\Phi\rangle \equiv N = N_0(0) + \sum_{\mathbf{k}\neq 0}\langle\Phi|a^\dagger_{\mathbf{k}}a_{\mathbf{k}}|\Phi\rangle$, can be easily expressed in terms of quasiparticle operators with Eq. (23), yielding $N = N_0(0) + \sum_{\mathbf{k}\neq 0} v_k^2$. A direct calculation gives

$$\frac{N'(0)}{N} \approx \frac{8}{3}\sqrt{\frac{na^3}{\pi}}, \tag{32}$$

which exhibits $\sqrt{na^3} \ll 1$ as the relevant dimensionless expansion parameter for a dilute Bose gas at low temperature. Note the fractional power $a^{3/2}$, which means that any simple perturbation expansion in powers of g

or a necessarily fails (this is where Bogoliubov's nonperturbative canonical transformation is so valuable).

1.2.2. Gross-Pitaevskii equation in a trap

In the Bogoliubov approximation, most of the particles remain in the condensate at low temperature. Thus, we start with the condensate wave function Ψ that describes the dilute system (we always assume $na^3 \ll 1$, which applies quite generally to atomic Bose condensates, but not to superfluid ^{4}He). Specifically, Ψ can be considered as an order parameter that characterizes the quantum-mechanical phase transition to the low-temperature ordered state. The Hamiltonian for the trapped condensate has the intuitive form

$$H = \int dV \left[\Psi^* \left(T + V_{\rm tr} \right) \Psi + \frac{1}{2} g |\Psi|^4 \right], \tag{33}$$

where T is the kinetic-energy operator and $V_{\rm tr}$ is the confining trap potential. The constraint of fixed number $\int dV \, |\Psi|^2 = N_0 \approx N$ is included with a Lagrange multiplier μ (which is the chemical potential), and the resulting Euler-Lagrange equation becomes the well-known Gross-Pitaevskii (GP) equation [9,10]

$$\left(T + V_{\rm tr} + V_H \right) \Psi = \mu \Psi, \tag{34}$$

where $V_H(\mathbf{r}) = gn(\mathbf{r})$ is the (now nonuniform) Hartree potential. More generally, the time-dependent condensate wave function obeys the time-dependent GP equation

$$i\hbar \frac{\partial \Psi}{\partial t} = \left(T + V_{\rm tr} + V_H \right) \Psi, \tag{35}$$

implying a time dependence $\propto \exp(-i\mu t/\hbar)$ for a stationary solution.

The time-dependent Gross-Pitaevskii equation takes a very intuitive quantum-hydrodynamic form when the condensate wave function is written as

$$\Psi(\mathbf{r}, t) = |\Psi(\mathbf{r}, t)| \, e^{iS(\mathbf{r}, t)}, \tag{36}$$

with the condensate density $n(\mathbf{r}, t) = |\Psi(\mathbf{r}, t)|^2$. The corresponding current density $\mathbf{j} = (\hbar/2Mi)[\Psi^* \boldsymbol{\nabla} \Psi - (\boldsymbol{\nabla} \Psi^*) \Psi]$ automatically assumes a hydrodynamic form $\mathbf{j} = n\mathbf{v}$, with an irrotational velocity

$$\mathbf{v} = \boldsymbol{\nabla} \Phi = \frac{\hbar \boldsymbol{\nabla} S}{M} \tag{37}$$

expressed in terms of a velocity potential $\Phi = \hbar S/M$.

Substitute Eq. (36) into the time-dependent GP equation, Eq. (35). The imaginary part yields the familiar continuity equation for compressible flow

$$\frac{\partial n}{\partial t} + \boldsymbol{\nabla} \cdot (n\mathbf{v}) = 0. \tag{38}$$

Correspondingly, the real part constitutes the analog of Bernoulli's equation for the condensate fluid

$$\frac{1}{2}Mv^2 + V_{\rm tr} + \frac{1}{\sqrt{n}}T\sqrt{n} + gn + M\frac{\partial \Phi}{\partial t} = 0. \tag{39}$$

To interpret this equation, recall that the Bernoulli equation for an irrotational compressible isentropic flow can be written very generally as[11]

$$\frac{1}{2}Mv^2 + V_{\rm tr} + \frac{e+p}{n} + M\frac{\partial \Phi}{\partial t} = 0, \tag{40}$$

where e is the internal energy density and p is the pressure, so that $e + p$ is the *enthalpy* density. The GP Hamiltonian, Eq. (33), identifies $e = \sqrt{n}T\sqrt{n} + \frac{1}{2}gn^2$, and the thermodynamic relation $p = -(\partial E/\partial V)_N$ implies that $p = \frac{1}{2}gn^2$. Consequently, the enthalpy per particle for the quantum hydrodynamics described by the GP equation is just

$$\frac{e+p}{n} = \frac{1}{\sqrt{n}}T\sqrt{n} + gn, \tag{41}$$

in agreement with Eq. (39). As a result, the zero-temperature condensate exhibits all the usual hydrodynamic behavior associated with classical nonviscous irrotational isentropic fluids, including the Kelvin circulation theorem that describes the dynamics of vortex lines.[11] The only explicit quantum-mechanical feature in Eq. (39) is the "quantum kinetic pressure" $(\sqrt{n})^{-1}T\sqrt{n}$ arising from spatial gradients in the particle density.

The behavior of a Bose condensate in a trap is considerably richer than in a box because of the additional energy scale and length scale associated with the single-particle ground state in the trap. In the case of an anisotropic harmonic trap, these are the oscillator energy $\sim \hbar\omega_0$ and the mean oscillator length $d_0 = \sqrt{\hbar/M\omega_0}$. The repulsive interactions tend to expand the condensate, leading to a mean radius R_0 that typically exceeds d_0. To illustrate the effect of the interactions, we can estimate the various terms of Eq. (33) for the interacting ground state. The kinetic energy per particle is of order $\langle T\rangle/N \sim \hbar^2/MR_0^2$, the trap potential energy per particle becomes $\langle V_{\rm tr}\rangle/N \sim M\omega_0^2 R_0^2$, and the Hartree energy per particle is of order

$\langle V_H \rangle / N \sim gn \sim \hbar^2 an/M \sim \hbar^2 aN/MR_0^3$. It is helpful to introduce the dimensionless expansion ratio $\mathcal{R} = R_0/d_0$, in which case the total ground-state energy E_g becomes

$$\frac{E_g}{N} \sim \hbar\omega_0 \left(\frac{1}{\mathcal{R}^2} + \mathcal{R}^2 + \frac{Na}{d_0} \frac{1}{\mathcal{R}^3} \right), \tag{42}$$

where we can take $\mathcal{R}$ as a variational parameter. Note the presence of the new dimensionless parameter Na/d_0, which arises from the additional length scale set by the trap. For $Na/d_0 \ll 1$, the system is essentially an ideal Bose gas, and the minimum occurs for $\mathcal{R} = 1$, which is the familiar harmonic-oscillator solution. For $Na/d_0 \gg 1$ (but still $na^3 \ll 1$), the repulsive interactions predominate and the kinetic energy is negligible because the condensate radius is significantly larger than the ideal-gas dimension d_0. Minimizing the last two terms of Eq. (42) gives the estimate $\mathcal{R}^5 \sim Na/d_0 \gg 1$. Thus the repulsive interactions expand the condensate according to

$$\frac{R_0}{d_0} \sim \begin{cases} 1, & \text{for } Na/d_0 \ll 1; \\ (Na/d_0)^{1/5}, & \text{for } Na/d_0 \gg 1. \end{cases} \tag{43}$$

A detailed analysis confirms these qualitative estimates, and we here concentrate on the limit of large interaction parameter $Na/d_0 \gg 1$, which is experimentally most relevant. Typical scattering lengths are a few nm (for example, $a = 2.75$ nm for ^{23}Na, $a = 5.77$ nm for ^{87}Rb, and $a = -1.45$ nm for ^{7}Li). Since d_0 is typically a few μm, the ratio Na/d_0 is large for $N \gg 10^3$ (typically, $N \sim 10^6$), and the mean condensate radius is of order $10d_0$. Thus the spatial gradients of the density are small, and the GP equation, Eq. (34), can be simplified by omitting the kinetic energy entirely. Equivalently, the condensate is taken as locally uniform, and this limit is therefore known as the Thomas-Fermi (TF) approximation [as is clear from the omission of the first term in Eq. (42)]. In the TF limit, the condensate density (and condensate wave function) is determined by an algebraic equation[12]

$$gn(\mathbf{r}) = g|\Psi(\mathbf{r})|^2 = \mu - V_{\rm tr}(\mathbf{r}), \tag{44}$$

where the right-hand side is positive and zero elsewhere. For the typical harmonic trap, the resulting density has a parabolic cross section and fills a (generally anisotropic) ellipsoid. The condensate's dimensions R_j ($j = x, y, z$) are determined by the classical turning points for a particle with energy μ

$$R_j^2 = \frac{2\mu}{M\omega_j^2}, \tag{45}$$

and the density thus becomes

$$n(\mathbf{r}) = n(0)\left(1 - \frac{x^2}{R_x^2} - \frac{y^2}{R_y^2} - \frac{z^2}{R_z^2}\right)\Theta\left(1 - \frac{x^2}{R_x^2} - \frac{y^2}{R_y^2} - \frac{z^2}{R_z^2}\right), \tag{46}$$

where $n(0) = \mu/g$ is the central density and Θ denotes the unit positive step function.

The normalization integral $\int dV n(\mathbf{r}) = N$ yields the important TF relation[12]

$$N = \frac{8\pi}{15} n(0) R_0^3 = \frac{R_0^5}{15\, a\, d_0^4}, \quad \text{or, equivalently,} \quad \frac{R_0^5}{d_0^5} = 15\frac{Na}{d_0} \gg 1, \tag{47}$$

where $R_0 = (R_x R_y R_z)^{1/3}$ is the mean TF condensate radius. This relation quantifies the previous estimate in Eq. (43). The TF chemical potential becomes

$$\mu = \frac{1}{2} M\omega_0^2 R_0^2 = \frac{1}{2}\hbar\omega_0 \frac{R_0^2}{d_0^2}, \tag{48}$$

so that $\mu \gg \hbar\omega_0$ in the TF limit (but still $\mu \ll k_B T_c \sim \hbar\omega_0 N^{1/3}$).

The TF limit leads to several important simplifications. For a trapped condensate, it is natural to define the healing length [Eq. (30)] in terms of the central density, with $\xi = [8\pi n(0)\, a]^{-1/2}$. In the TF limit, this choice implies that

$$\xi\, R_0 = d_0^2, \quad \text{or, equivalently,} \quad \frac{\xi}{d_0} = \frac{d_0}{R_0} \ll 1. \tag{49}$$

Thus the TF limit ($Na/d_0 \gg 1$) provides a clear separation of length scales $\xi \ll d_0 \ll R_0$, and the (small) healing length ξ will be seen to characterize the size of the vortex core. In contrast, the healing length formally diverges in the near-ideal limit ($Na/d_0 \ll 1$) but the vortex core size remains comparable with d_0 and hence with the size of the condensate.

The quantum-hydrodynamic equations also simplify in the TF limit, because the quantum kinetic pressure in Eq. (39) becomes negligible. For the static TF ground-state density given in Eq. (44), the small perturbations n' in the density and Φ' in the velocity potential can be combined to yield the generalized wave equation[13]

$$M\frac{\partial^2 n'}{\partial t^2} = \boldsymbol{\nabla}\cdot\left[(\mu - V_{\text{tr}})\,\boldsymbol{\nabla} n'\right] \quad \text{or, equivalently,} \quad \frac{\partial^2 n'}{\partial t^2} = \boldsymbol{\nabla}\cdot\left[s^2(\mathbf{r})\boldsymbol{\nabla} n'\right], \tag{50}$$

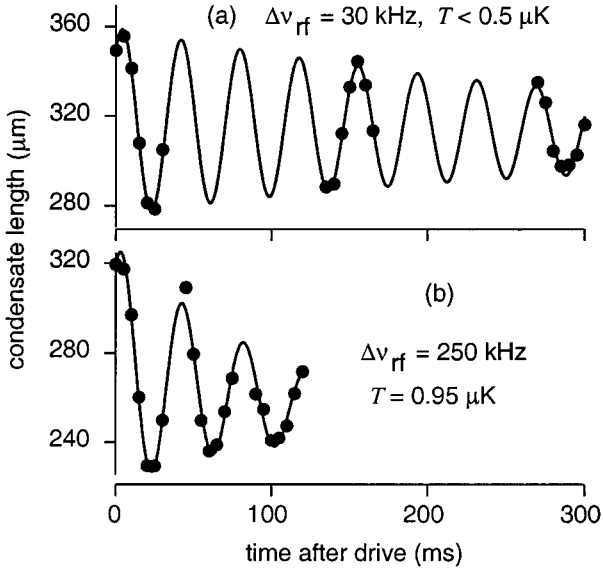

Fig. 2. Oscillations of the axial width of the condensate in the cigar-shaped trap at MIT. The excited collective motion is the low-lying $m = 0$ mode, shown at (a) low and (b) high temperature (from Ref. 14).

where $s^2(\mathbf{r}) = [\mu - V_{\rm tr}(\mathbf{r})]/M$ defines a spatially varying local sound speed. Stringari has used this equation to analyze the low-lying normal modes of the TF condensate, and several experimental studies have verified these predictions in considerable detail (see, for example, Ref. 2 and Fig. 2).

1.2.3. Bogoliubov equations for small-amplitude perturbations

An interacting Bose gas can be described by second-quantized field operators[5] $\hat{\psi}(\mathbf{r})$ and $\hat{\psi}^\dagger(\mathbf{r})$ that obey the commutation relations $[\hat{\psi}(\mathbf{r}), \hat{\psi}^\dagger(\mathbf{r}')] = \delta(\mathbf{r} - \mathbf{r}')$, $[\hat{\psi}(\mathbf{r}), \hat{\psi}(\mathbf{r}')] = [\hat{\psi}^\dagger(\mathbf{r}), \hat{\psi}^\dagger(\mathbf{r}')] = 0$. In the Bogoliubov approximation at zero temperature, these quantum field operators are replaced by "classical" wave functions Ψ and Ψ^* that obey the GP equation. More generally, the second-quantized Bose field operator $\hat{\psi}$ can be written as $\hat{\psi}(\mathbf{r}) \approx \Psi(\mathbf{r}) + \hat{\phi}(\mathbf{r})$, where $\hat{\phi}$ is a small deviation operator from the macroscopic condensate wave function Ψ. These deviation operators obey the approximate Bose-Einstein commutation relations

$$\left[\hat{\phi}(\mathbf{r}), \hat{\phi}^{\dagger}(\mathbf{r}')\right] \approx \delta(\mathbf{r}-\mathbf{r}'), \quad \left[\hat{\phi}(\mathbf{r}), \hat{\phi}(\mathbf{r}')\right] = \left[\hat{\phi}^{\dagger}(\mathbf{r}), \hat{\phi}^{\dagger}(\mathbf{r}')\right] \approx 0. \tag{51}$$

Since $\hat{\phi}(\mathbf{r})$ does not conserve particle number, it is convenient to use a grand canonical ensemble, with the new Hamiltonian operator $\hat{K} = \hat{H} - \mu\hat{N}$. To leading (second) order in the small deviations, the perturbation in $\hat{K}$ contains not only the usual "diagonal" terms involving $\hat{\phi}^{\dagger}\hat{\phi}$, but also "off-diagonal" terms proportional to $\hat{\phi}\hat{\phi}$ and $\hat{\phi}^{\dagger}\hat{\phi}^{\dagger}$ [compare with Eq. (20) for a uniform system in a box]. Consequently, the resulting Heisenberg operators $\hat{\phi}$ and $\hat{\phi}^{\dagger}$ obey coupled linear equations of motion (it is here that the role of the condensate is evident, for this coupling vanishes if Ψ vanishes). Pitaevskii[10] developed this approach for the particular case of a vortex line in an unbounded condensate, and the formalism was subsequently extended to include a general nonuniform condensate.[15,16]

In direct analogy to the Bogoliubov transformation for the uniform system, assume the existence of a linear transformation to quasiparticle operators α_j and $\alpha_j^{\dagger}$ for a set of normal modes labeled by j

$$\hat{\phi}(\mathbf{r}, t) = \sum_j{}' \left[u_j(\mathbf{r})\alpha_j(t) - v_j^*(\mathbf{r})\alpha_j^{\dagger}(t)\right], \tag{52}$$

$$\hat{\phi}^{\dagger}(\mathbf{r}, t) = \sum_j{}' \left[u_j^*(\mathbf{r})\alpha_j^{\dagger}(t) - v_j(\mathbf{r})\alpha_j(t)\right], \tag{53}$$

where the primed sum means to omit the condensate mode. Here, the quasiparticle operators α_j and $\alpha_k^{\dagger}$ obey Bose-Einstein commutation relations $\left[\alpha_j, \alpha_k^{\dagger}\right] = \delta_{jk}$ and have simple harmonic time dependences $\alpha_j(t) = \alpha_j \exp(-iE_jt/\hbar)$ and $\alpha_j^{\dagger}(t) = \alpha_j^{\dagger} \exp(iE_jt/\hbar)$. Comparison with the equations of motion for $\hat{\phi}$ and $\hat{\phi}^{\dagger}$ shows that the corresponding spatial amplitudes obey a set of coupled linear "Bogoliubov equations"

$$Lu_j - g(\Psi)^2 v_j = E_j u_j, \tag{54}$$

$$Lv_j - g(\Psi^*)^2 u_j = -E_j v_j, \tag{55}$$

where

$$L = T + V_{\mathrm{tr}} - \mu + 2g|\Psi|^2 \tag{56}$$

is a Hermitian operator.

Straightforward manipulations with the Bogoliubov equations show that $E_j \int dV \left(|u_j|^2 - |v_j|^2\right)$ is real. If the integral $\int dV \left(|u_j|^2 - |v_j|^2\right)$ is nonzero,

then E_j itself is real. As in the case of a uniform condensate, the Bose-Einstein commutation relations, Eq. (51), for the deviations from the nonuniform condensate can be shown to imply the following *positive* normalization[15]

$$\int dV \left(|u_j|^2 - |v_j|^2\right) = 1. \tag{57}$$

For each solution u_j, v_j with eigenvalue E_j and positive normalization, the Bogoliubov equations always have a second solution v_j^*, u_j^* with eigenvalue $-E_j$ and *negative* normalization. The only exception to the requirement of real eigenvalues arises for zero-norm solutions with $\int dV \left(|u_j|^2 - |v_j|^2\right) = 0$. In this case the character of the eigenvalue requires additional analysis.

In terms of the quasiparticle operators, the approximate perturbation Hamiltonian operator takes the simple intuitive form

$$\hat{K}' \approx \sum_j{}' E_j \, \alpha_j^\dagger \alpha_j, \tag{58}$$

apart from a constant ground-state contribution of all the normal modes. Here, the sum is over all the states with positive normalization, and it is clear that the sign of the energy eigenvalues E_j is crucial for the stability. If one or more of the eigenvalues is negative, the Hamiltonian is no longer positive definite, and the system can lower its energy by creating quasiparticles associated with the unstable modes.

The present derivation of the Bogoliubov equations and their properties emphasizes the quantum-mechanical basis for the positive normalization condition, Eq. (57), and the sign of the eigenvalues. It is worth noting an alternative purely "classical" treatment[2] based directly on small perturbations of the time-dependent GP equation, Eq. (35), around the static condensate $\Psi(\mathbf{r})$. The solution is assumed to have the form

$$\Psi(\mathbf{r}, t) = e^{-i\mu t/\hbar} \left[\Psi(\mathbf{r}) + u(\mathbf{r}) e^{-i\omega t} - v^*(\mathbf{r}) e^{i\omega t}\right], \tag{59}$$

and the appropriate eigenvalue equations then reproduce Eqs. (54) and (55).

For a uniform condensate, the solutions of Eqs. (54) and (55) are plane waves, and the corresponding energy is the celebrated Bogoliubov spectrum[7]

$$E_k = \sqrt{gn\hbar^2 k^2/M + \left(\hbar^2 k^2/2M\right)^2}, \tag{60}$$

where $\mathbf{k}$ is the wave vector of the excitation and n is the condensate density, as found previously in Eq. (25) with a canonical transformation. For long wavelengths $k\xi \ll 1$, Eq. (60) reduces to a linear phonon spectrum $E_k \approx \hbar s k$ with the speed of compressional sound $s = \sqrt{gn/M}$ given by Eq. (29).

To emphasize the importance of the sign of the eigenfrequency, it is instructive to consider an unbounded condensate that moves uniformly with velocity $\mathbf{v}$. The condensate wave function is $\Psi(\mathbf{r}) = \sqrt{n}\, e^{i\mathbf{q}\cdot\mathbf{r}}$, where $\mathbf{q} = M\mathbf{v}/\hbar$ and the chemical potential becomes $\mu = \frac{1}{2}Mv^2 + gn$. The Bogoliubov amplitudes for an excitation with wave vector $\mathbf{k}$ relative to the moving condensate have the form

$$\begin{pmatrix} u_{\mathbf{k}}(\mathbf{r}) \\ v_{\mathbf{k}}(\mathbf{r}) \end{pmatrix} = \begin{pmatrix} e^{i\mathbf{q}\cdot\mathbf{r}} u_k e^{i\mathbf{k}\cdot\mathbf{r}} \\ e^{-i\mathbf{q}\cdot\mathbf{r}} v_k e^{i\mathbf{k}\cdot\mathbf{r}} \end{pmatrix}, \tag{61}$$

where the different signs $\pm i\mathbf{q}\cdot\mathbf{r}$ arise from the different phases $\pm i2\mathbf{q}\cdot\mathbf{r}$ in the off-diagonal coupling terms in the Bogoliubov equations [Eqs. (54) and (55)]. The solution with positive norm has the eigenvalue

$$E_{\mathbf{k}}(\mathbf{v}) = \hbar\mathbf{k}\cdot\mathbf{v} + E_k. \tag{62}$$

In the long-wavelength limit, this excitation energy reduces to $E_{\mathbf{k}}(\mathbf{v}) \approx \hbar k(v\cos\theta + s)$, where θ is the angle between $\mathbf{k}$ and $\mathbf{v}$. For $v < s$ the quasiparticle energy is positive for all angles θ, but for $v > s$ the quasiparticle energy becomes negative for certain directions, indicating the onset of an instability. This behavior simply reflects the well-known Landau critical velocity for the onset of dissipation, associated with the emission of quasiparticles. For $v > s$, the GP description becomes incomplete because the excitation of quasiparticles means that the noncondensate is no longer negligible. Note that the repulsive interactions produce the linear (phonon) long-wavelength spectrum for $k \lesssim \xi^{-1} \propto \sqrt{g}$. It is this feature that leads to the finite speed of sound (and thus finite Landau critical velocity). In this sense, the repulsive interactions are essential for the stability of a dilute Bose gas, because an ideal uniform Bose gas would have $s = 0$ and therefore $v_c = 0$.

A uniform Bose gas with attractive interactions (for example, ^{7}Li) would be intrinsically unstable because the speed of sound is imaginary. The situation is different in a trap, where the finite size of the condensate quantizes the allowed wave numbers. For negative $a = -|a|$, the Bogoliubov spectrum becomes $E_k^2 = (\hbar^2/2M)^2 k^2(k^2 - 16\pi n|a|)$, which is negative (and therefore unstable) in the interval $k^2 < 16\pi n|a|$. For a finite condensate with mean radius R_0, however, the minimum allowed wavenumber is $k_{\min} \approx \pi/R_0$. Hence the system can remain stable if $\pi^2/R_0^2 \gtrsim 16\pi n|a|$. Since the density of is order $n \sim N/R_0^3$, this analysis predicts the critical number

$$N_c \approx \frac{\pi}{16}\frac{R_0}{|a|} \approx \frac{\pi}{16}\frac{d_0}{|a|}, \tag{63}$$

because $R_0 \approx d_0$ for such a small value of the ratio $N_c|a|/d_0 \approx \pi/16$. For

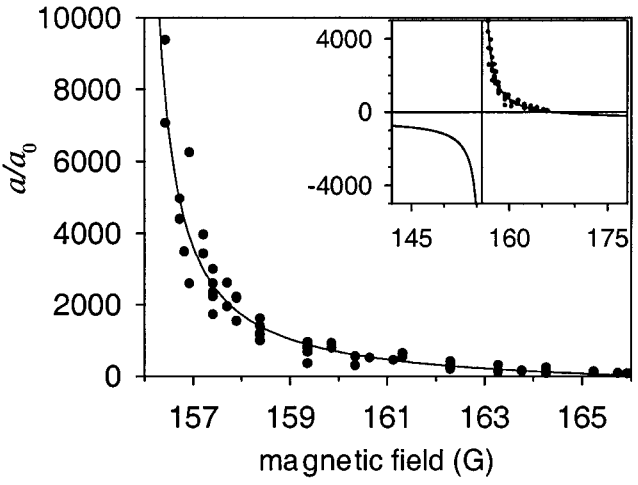

Fig. 3. Scattering length for ^{85}Rb in units of the Bohr radius (a_0) as a function of the magnetic field. For reference, the shape of the full resonance is shown in the inset (from Ref. 18).

$N \lesssim N_c$, the positive kinetic energy arising from the confinement stabilizes a trapped condensate with attractive interactions. For $N \gtrsim N_c$, however, the attractive interaction energy predominates, and the condensate is expected to collapse. Experiments with ^{7}Li have measured a critical number N_c in reasonable agreement with detailed estimates based on the GP equation.[17]

Recently, it has become possible to "tune" the scattering length in certain hyperfine states by varying an applied magnetic field (this phenomenon occurs through what is known as a Feshbach resonance). In particular, the boson isotope ^{85}Rb has been studied in detail.[18–20] In zero magnetic field, the scattering length is negative, and it undergoes a resonant behavior at $B \approx 155$ G, when $a(B)$ goes discontinuously from $-\infty$ to $+\infty$ (see Fig. 3; note that the phase shift and the s-wave contribution to the scattering amplitude are continuous at this point). For larger B, the scattering length decreases rapidly from $+\infty$ and changes from positive to negative at $B \approx 166$ G. The system then exhibits a collapse when $|a|$ reaches the critical value appropriate for the given N. For a sudden quench into the unstable regime, the subsequent explosions display anisotropic bursts and other phenomena that challenge current theoretical models.

In addition to the possibility of initiating a collapse by switching a from positive to negative, the Feshbach resonance means that the scattering length can be significantly larger than the typical repulsive values $a \sim$ a few

nm for ^{23}Na and ^{87}Rb. Thus the small dimensionless parameter $\sqrt{na^3}$ can in principle produce a significant correction to the nearly ideal-gas behavior. This possibility is only now just beginning to be explored for a dilute Bose gas in a trap.

In the last year, two separate groups have produced BEC with metastable ^{4}He in the lowest $2\,^3S_1$ spin-triplet state.[21,22] Although the results are still somewhat preliminary, they suggest a large scattering length $a \approx 20$ nm, which also could make possible the study of corrections associated with a nonzero gas parameter na^3.

2. VORTICES IN A TRAPPED DILUTE BOSE-EINSTEIN CONDENSATE

The Gross-Pitaevskii (GP) equation serves as the basis for most theoretical analyses of vortices in a Bose condensate at low temperatures. Although many studies had predicted the presence and behavior of such vortices, experimental confirmation has appeared only a few years ago.[23,24] For a recent review of most of these questions, see Ref. 25. We have already remarked that the time-dependent GP equation is wholly equivalent to the hydrodynamics of an irrotational nonviscous compressible isentropic fluid. As such, it necessarily incorporates the characteristic aspects of classical vortices, and it is convenient first to review some of these features.

2.1. Vortex Line in an Unbounded Condensate

Gross[9] and Pitaevskii[10] considered a singly quantized straight vortex in a condensate with bulk particle density n, assuming a wave function of the form $\Psi(\mathbf{r}) = \sqrt{n}\,\chi(\mathbf{r})$, with

$$\chi(\mathbf{r}) = e^{i\phi} f\left(\frac{r_\perp}{\xi}\right), \tag{64}$$

where $(r_\perp, \phi)$ are two-dimensional cylindrical polar coordinates, and $f \to 1$ for $r_\perp \gg \xi$. Equation (37) immediately gives the local circulating flow velocity

$$\mathbf{v} = \frac{\hbar}{M r_\perp}\,\hat{\phi}, \tag{65}$$

which represents circular streamlines with an amplitude that becomes large as $r_\perp \to 0$. Since the speed of sound in a dilute Bose gas is $s = \sqrt{\mu/M} = \hbar/\sqrt{2}M\xi$, the circulating flow velocity becomes supersonic near the vortex

core when $r_\perp \approx \xi$. In this sense, the vortex core is associated with local cavitation.

The particular condensate wave function Eq. (64) describes an infinite straight vortex line with quantized circulation

$$\kappa = \oint d\mathbf{l} \cdot \mathbf{v} = \frac{h}{M}. \tag{66}$$

Stokes's theorem then yields $h/M = \int d\mathbf{S} \cdot \boldsymbol{\nabla} \times \mathbf{v}$, with the corresponding localized vorticity

$$\boldsymbol{\nabla} \times \mathbf{v} = \frac{h}{M}\, \delta^{(2)}(\mathbf{r}_\perp)\, \hat{z}. \tag{67}$$

Hence the velocity field around a vortex in a dilute Bose condensate is irrotational except for a singularity at the origin.

The kinetic energy per unit length is given by

$$\int d^2 r_\perp\, \Psi^* \left(-\frac{\hbar^2 \nabla^2}{2M} \right) \Psi = \frac{\hbar^2}{2M} \int d^2 r_\perp\, |\boldsymbol{\nabla} \Psi|^2 = \frac{\hbar^2 n}{2M} \int d^2 r_\perp \left[\left(\frac{df}{dr_\perp} \right)^2 + \frac{f^2}{r_\perp^2} \right], \tag{68}$$

and the centrifugal barrier in the second term forces the amplitude to vanish linearly within a core of radius $\approx \xi$ (see Fig. 4). This core structure ensures that the particle current density $\mathbf{j} = n\mathbf{v}$ vanishes and the total kinetic-energy density remains finite as $r_\perp \to 0$. The presence of the vortex produces an additional energy E_v per unit length, both from the kinetic energy of circulating flow and from the local compression of the fluid. Numerical analysis with the GP equation yields $E_v \approx (\pi \hbar^2 n/M) \ln (1.46 R/\xi)$, where R is an outer cutoff; apart from the additive numerical constant, this value is simply the integral of $\frac{1}{2} M v^2 n$.

In the context of rotating superfluid ^{4}He, Feynman[26] noted that solid-body rotation with $\mathbf{v}_{\rm sb} = \boldsymbol{\Omega} \times \mathbf{r}$ has constant vorticity $\boldsymbol{\nabla} \times \mathbf{v}_{\rm sb} = 2\boldsymbol{\Omega}$. Since each quantized vortex line in rotating superfluid ^{4}He has an identical localized vorticity associated with the singular circulating flow, Eq. (67), he argued that a uniform array of vortices can "mimic" solid-body rotation on average, even though the flow is strictly irrotational away from the cores. He then considered the circulation $\Gamma = \oint_C d\mathbf{l} \cdot \mathbf{v}$ along a closed contour C enclosing a large number $\mathcal{N}_v$ of vortices. The quantization of circulation ensures that $\Gamma = \mathcal{N}_v \cdot \kappa$, where $\kappa = h/M$ is the quantum of circulation. If the vortex array mimics solid-body rotation, however, the circulation should also be $\Gamma = 2\Omega \cdot \mathcal{A}_v$, where $\mathcal{A}_v$ is the area enclosed by the contour C. In this way, the areal vortex density in a rotating superfluid becomes

$$n_v = \frac{\mathcal{N}_v}{\mathcal{A}_v} = \frac{2\Omega}{\kappa}. \tag{69}$$

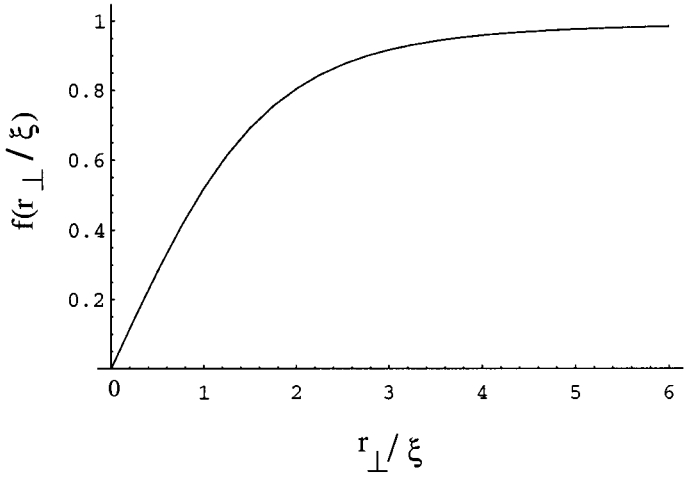

Fig. 4. Radial wave function $f(r_\perp/\xi)$ obtained by numerical solution of the stationary GP equation for a straight vortex line (from Ref. 25).

Equivalently, the area per vortex $1/n_v = \kappa/2\Omega \equiv \pi b^2$ can be taken to define the intervortex spacing b, which decreases with increasing rotation speed like $1/\sqrt{\Omega}$. Note that Eq. (69) is directly analogous to the density of vortices (flux lines) $n_v = B/\Phi_0$ in a type-II superconductor, where B is the magnetic flux density and $\Phi_0 = h/2e$ is the quantum of magnetic flux in SI units (see, for example, Ref. 27).

To illustrate that the time-dependent GP equation indeed incorporates the correct classical vortex dynamics, consider a state of the form

$$\Psi(\mathbf{r},t) = \sqrt{n}\, e^{i\mathbf{q}\cdot\mathbf{r}}\, \chi(\mathbf{r}-\mathbf{r}_0)\, e^{-i\mu t/\hbar}, \tag{70}$$

where χ is the previous stationary solution [Eq. (64)] of the GP equation for a quantized vortex, now shifted to the instantaneous position $\mathbf{r}_0(t)$, and μ is a modified chemical potential. The total flow velocity is the sum of a uniform velocity $\mathbf{v}_0 = \hbar\mathbf{q}/M$ and the circulating flow around the vortex. Substitute this wave function into the time-dependent GP equation, Eq. (35). Since χ itself obeys the stationary GP equation, Eq. (34), with chemical potential gn, a straightforward analysis shows that $\mu = \frac{1}{2}Mv_0^2 + gn$, where the first term arises from the center of mass motion of the condensate. The remaining terms yield

$$i\hbar\frac{\partial\chi(\mathbf{r}-\mathbf{r}_0)}{\partial t} \equiv -i\hbar\frac{d\mathbf{r}_0}{dt}\cdot\nabla\chi(\mathbf{r}-\mathbf{r}_0) = -i\hbar\mathbf{v}_0\cdot\nabla\chi(\mathbf{r}-\mathbf{r}_0). \tag{71}$$

This equation shows that $d\mathbf{r}_0(t)/dt = \mathbf{v}_0$, so that the vortex wave function moves rigidly with the applied flow velocity $\mathbf{v}_0$, correctly reproducing the result from classical irrotational hydrodynamics that each element of a vortex moves with the local velocity at its particular location. More generally, in the presence of several straight vortex lines, each line moves with the velocity generated by all the other vortices, again in agreement with the classical result.

2.2. Vortex Line in a Trap

Consider an axisymmetric trap with oscillator frequencies $\omega_\perp$ and ω_z. For $\omega_z/\omega_\perp > 1$, the condensate has a flattened disk shape, whereas for $\omega_z/\omega_\perp < 1$, the condensate has an elongated cigar shape. The axisymmetry means that the angular momentum L_z is conserved, allowing a simple classification of the various states. In the case of a singly quantized vortex on the symmetry axis, the condensate wave function has the form

$$\Psi(\mathbf{r}) = e^{i\phi}\,|\Psi(r_\perp, z)|. \tag{72}$$

The circulating velocity field is the same as Eq. (65), and the centrifugal energy again forces the wave function to vanish near $r_\perp \lesssim \xi$, yielding a toroidal condensate density. This behavior is especially clear in the TF limit ($Na/d_0 \gg 1$), when the density becomes

$$n(r_\perp, z) \approx n(0)\left(1 - \frac{\xi^2}{r_\perp^2} - \frac{r_\perp^2}{R_\perp^2} - \frac{z^2}{R_z^2}\right)\Theta\left(1 - \frac{\xi^2}{r_\perp^2} - \frac{r_\perp^2}{R_\perp^2} - \frac{z^2}{R_z^2}\right), \tag{73}$$

where Θ is the unit positive step function. This expression differs from Eq. (46) for a vortex-free condensate only because of the centrifugal barrier $\xi^2/r_\perp^2$, which forces the density to vanish within a core of radius $\approx \xi$ that flares out away from the center of the trap. The TF separation of length scales $\xi/d_0 = d_0/R_0 \ll 1$ means that the vortex affects the density only near the core region; hence the density can be assumed to be the same as for a vortex-free condensate with a suitable short-distance cutoff near the core.

If the condensate is in rotational equilibrium at an angular velocity Ω, then the Hamiltonian H in Eq. (33) must be altered to $H' = H - \Omega L_z = H + \int dV\, \Psi^*(i\hbar\Omega\hat{z}\cdot\mathbf{r}\times\boldsymbol{\nabla})\,\Psi = H + i\hbar\Omega \int dV\, \Psi^*(\partial\Psi/\partial\phi)$. Let $E_0'(\Omega)$ denote the energy of the rotating vortex-free condensate, and $E_1'(r_0, \Omega)$ the corresponding energy of a rotating condensate containing a straight vortex that is displaced laterally from the symmetry axis by a distance r_0. This latter

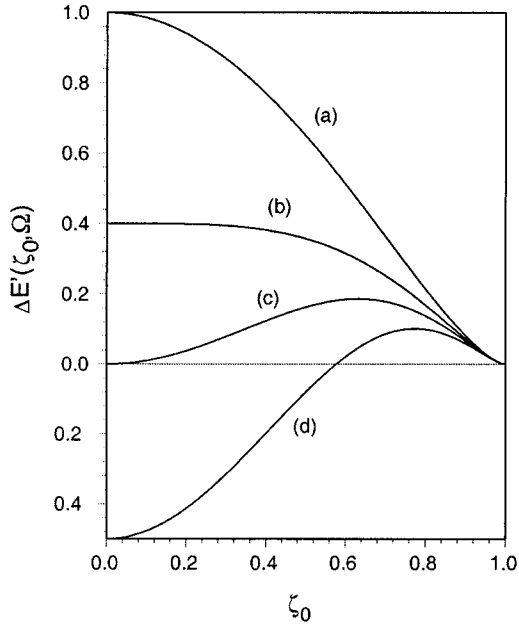

Fig. 5. Vortex energy [in units of $\Delta E'(0,0)$] associated with a singly quantized straight vortex in a rotating axisymmetric trap in the TF limit as a function of fractional displacement ζ_0 from the trap's central axis. Different curves represent different fixed values of the external angular velocity Ω: (a) $\Omega = 0$ (unstable); (b) $\Omega = \Omega_m$ (onset of metastability at the origin); (c) $\Omega = \Omega_c$ (onset of stability at the origin); (d) $\Omega = \frac{3}{2}\Omega_c$, where thin barrier inhibits vortex tunneling in from the surface (from Ref. 25).

quantity includes the additional energy of the circulating flow. The assumption of a straight vortex line means that this description holds best for a disk-shaped condensate with $\omega_z \gtrsim \omega_\perp$. The difference between these two energies $\Delta E'(r_0,\Omega) = E_1'(r_0,\Omega) - E_0'(\Omega)$ represents the energy associated with the formation of the vortex; for fixed Ω, the dependence on r_0 characterizes the local and global stability of the vortex near the trap center.

A detailed calculation with logarithmic accuracy for an axisymmetric TF condensate gives[28]

$$\Delta E'(r_0,\Omega) = \frac{8\pi}{3}\,\mu R_z \xi^2\, n(0)\left[\ln\left(\frac{R_\perp}{\xi}\right)\left(1-\zeta_0^2\right)^{3/2} - \frac{2M\Omega R_\perp^2}{5\hbar}\left(1-\zeta_0^2\right)^{5/2}\right], \tag{74}$$

where $\zeta_0 = r_0/R_\perp$ is a dimensionless lateral displacement. This vortex en-

ergy is shown in Fig. 5 as a function of ζ_0 for various fixed values of Ω. Curve (a) for $\Omega = 0$ shows that the corresponding energy $\Delta E'(\zeta_0, \Omega = 0)$ decreases monotonically with increasing ζ_0, and that the curvature is negative at $\zeta_0 = 0$. In the absence of dissipation, energy is conserved and the vortex follows a circular trajectory at fixed ζ_0 around the center of the trap along a line $V_{\rm tr} = \text{const}$ at an angular speed proportional to $-\partial \Delta E'/\partial \zeta_0$. At low but finite temperature, however, the vortex experiences weak dissipation; thus it slowly reduces its energy by moving outward along curve (a), executing a spiral trajectory in the xy plane.

With increasing fixed rotation speed Ω, the function $\Delta E'(\zeta_0, \Omega)$ flattens for small $\zeta_0 \ll 1$. Curve (b) shows the special case of zero curvature at $\zeta_0 = 0$. It corresponds to the rotation speed

$$\Omega_m = \frac{3}{2} \frac{\hbar}{M R_\perp^2} \ln\left(\frac{R_\perp}{\xi}\right) \tag{75}$$

at which angular velocity a central vortex first becomes metastable in a large disk-shaped condensate. For $\Omega < \Omega_m$, the negative local curvature at $\zeta_0 = 0$ means that weak dissipation impels the vortex away from the center. For $\Omega > \Omega_m$, however, the positive local curvature means that weak dissipation now impels the vortex back toward the center of the trap. In this regime, the central position is *locally* stable; it is not *globally* stable, however, because $\Delta E'(0, \Omega)$ is positive for $\Omega \approx \Omega_m$.

Curve (c) shows that $\Delta E'(0, \Omega_c)$ vanishes at the thermodynamic critical angular velocity

$$\Omega_c = \frac{5}{2} \frac{\hbar}{M R_\perp^2} \ln\left(\frac{R_\perp}{\xi}\right) = \frac{5}{3} \Omega_m. \tag{76}$$

For $\Omega > \Omega_c$, the central vortex is both locally and globally stable relative to the vortex-free state, and the energy barrier near the outer surface of the condensate becomes progressively narrower with increasing Ω. Curve (d) illustrates this behavior for $\Omega = \frac{3}{2}\Omega_c$. Eventually, the barrier thickness becomes comparable with the thickness of the boundary layer within which the TF approximation fails, and it has been suggested that a vortex might then nucleate spontaneously through a surface instability.

2.3. Experimental Creation and Detection of Vortices

The first experimental detection of a vortex involved a nearly spherical ^{87}Rb TF condensate containing two different internal (hyperfine) components[23] that tend to separate into immiscible phases. The JILA group in Boulder

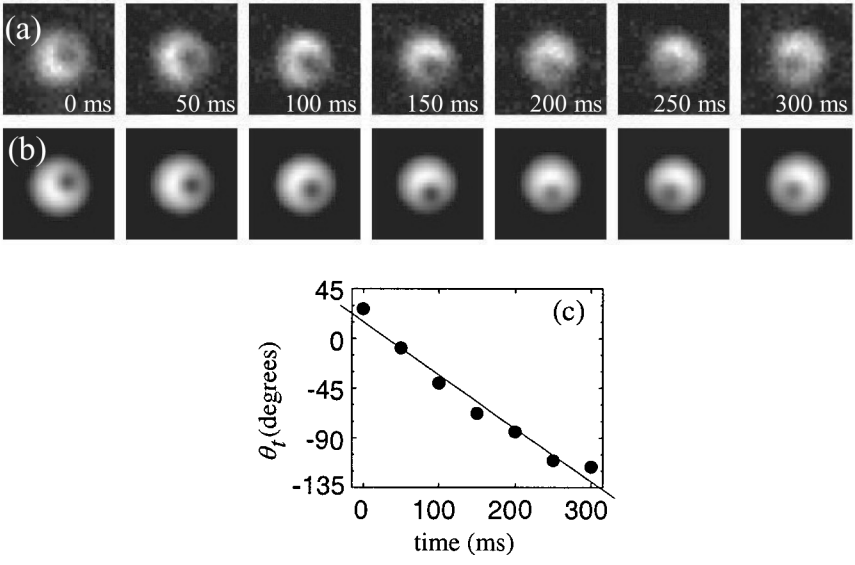

Fig. 6. (a) Successive images of a "two-component" condensate with a vortex in one component. The recorded profile of each trapped condensate is fit with a smooth TF distribution in (b). The vortex core is the dark region within the bright condensate image. (c) The azimuthal angle of the core is determined for each image, and plotted vs. time held in the trap. A linear fit to the data gives a precession frequency 1.3(1) Hz (from Ref. 29).

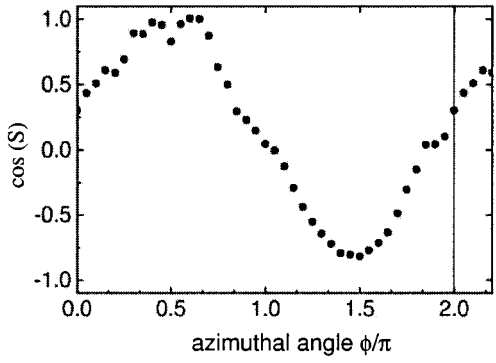

Fig. 7. Cosine of the phase around the vortex, showing the sinusoidal variation expected for the azimuthal angle (from Ref. 23).

created the vortex through a somewhat intricate coherent process that controlled the interconversion between the two components (discussed below in Section 3). They were able to spin up the condensate by coupling the two components and applying a suitable stirring perturbation. They then turned off the coupling, leaving the system with a residual trapped quantized vortex consisting of one circulating component surrounding a nonrotating core of the other component, whose size is determined by the relative fraction of the two components. By selective tuning, they can image either component nondestructively;[29] Figure 6 shows the precession of the filled vortex core around the trap center. In addition, an interference procedure allowed them to map the variation of the cosine of the phase around the vortex, clearly showing the expected sinusoidal variation (Fig. 7).

The JILA group has also been able to remove the component filling the core, in which case they obtain a single-component vortex.[29] This one-component vortex has a smaller core size and can be imaged only by expanding both the condensate and the core, which becomes visible through its reduced density. They first make an image of the two-component vortex, next remove the component filling the core, and then make an image of the expanded one-component vortex after a variable time delay. In this way, they can measure the precession rate of the one-component empty-core vortex and compare it with theoretical predictions.[30] The data show no tendency for the core to spiral outward, suggesting that the thermal damping is negligible on the time scale of ~ 1 s.

Separately, the ENS group in Paris observed the formation of one and more vortices in a single-component ^{87}Rb elongated cigar-shaped TF condensate with a weak nonaxisymmetric deformation that rotates about its

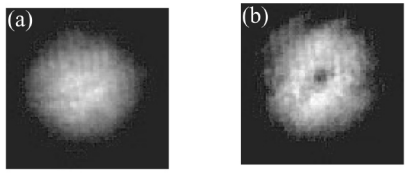

Fig. 8. Optical thickness of the expanded cloud in the transverse direction showing the difference between the states (a) without and (b) with a vortex (from Ref. 31). Reprinted with permission from Journal of Modern Optics copyright Taylor and Francis Ltd.

long axis.[24,31,32] In essence, a static cylindrically symmetric magnetic trap is augmented by a nonaxisymmetric attractive dipole potential created by a stirring laser beam. The combined potential produces a cigar-shaped harmonic trap with a slightly anisotropic transverse profile. The transverse anisotropy rotates slowly at a rate $\Omega \lesssim 200$ Hz. In the first experiments,[24] the trap was rotated in the normal state and then cooled, with the clear signal of the vortex shown in Fig. 8 (the trap was turned off, allowing the atomic cloud to expand so that the vortex core becomes visible). This order was reversed (cool first, then rotate) in a later series of runs.[32] In both cases, the observed critical angular velocity $\sim 0.7\omega_\perp$ for creating the first (central) vortex was roughly 70% higher than the predicted thermodynamic value Ω_c in Eq. (76). These observations confirm the suggestion that a surface instability could nucleate a vortex, which is predicted to occur at $\Omega = \omega_\perp/\sqrt{2}$ for a quadrupole deformation with $l = 2$.[33,34] Subsequent experiments[35,36] at ENS confirm the predictions in considerable detail and have also seen lower nucleation frequencies associated with surface waves corresponding to the higher harmonic $l = 3$ (for general l, the surface instability, has a frequency $\omega_\perp/\sqrt{l}$).

The ENS group has also detected vortex arrays[31] with up to 11 vortex lines arranged in two concentric rings. These patterns are reminiscent of those predicted and seen in rotating superfluid ^{4}He.[37] More recently, the MIT group has made significantly larger rotating condensates in less elongated traps.[38] As shown in Fig. 9, they have observed remarkably regular triangular arrays with up to 130 vortices, directly analogous to the Abrikosov lattice of quantized flux lines in type-II superconductors.[27]

Recently, several groups have studied the behavior of a rapidly rotating condensate.[39,40] This question is of interest because the external rotation Ω induces a repulsive centrifugal potential $V_{\text{cent}}(r) = -\frac{1}{2}M\Omega^2 r_\perp^2$ that opposes the attractive trap potential $V_\perp(r) = \frac{1}{2}M\omega_\perp^2 r_\perp^2$. Indeed, the physics

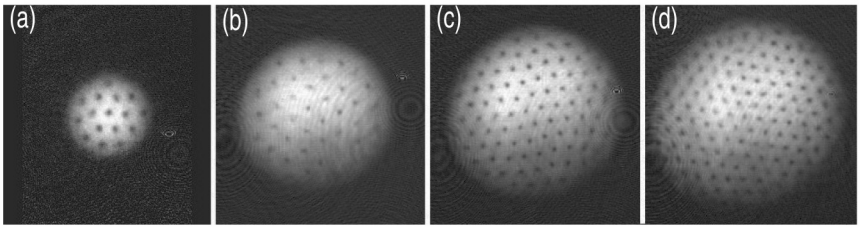

Fig. 9. Observation of vortex lattices. The examples shown contain (a) 16 (b) 32 (c) 80 and (d) 130 vortices. The vortices have "crystallized" in a triangular pattern. The diameter of the cloud in (d) was 1 mm after ballistic expansion, which represents a magnification of 20 (from Ref. 38). Reprinted with permission from Science copyright American Association for the Advancement of Science.

is predicted to become qualitatively different when $\Omega \to \omega_\perp$,[41–43] although such a limit is not yet attainable. To understand the basic effect, note that the combined radial potential $V_{\rm cent}(r) + V_\perp(r) = \frac{1}{2}M(\omega_\perp^2 - \Omega^2)r_\perp^2$ represents a confining potential with an effective renormalized trap frequency $\omega_{\rm eff} = \sqrt{\omega_\perp^2 - \Omega^2}$. As a result, the TF condensate radius in a rotating condensate $R_\perp(\Omega)$ increases like $R_\perp(\Omega)/R_\perp(0) = [1 - (\Omega/\omega_\perp)^2]^{-3/10}$, and the MIT experiments[39] have observed this altered aspect ratio. In contrast, the JILA group[40] starts from a rotating normal cloud and cools to create a rotating BEC with an associated superfluid vorticity. In this latter approach, the altered aspect ratio serves to measure the effective angular velocity of the rotating condensate.

2.4. Bogoliubov Equations: Stability of Small-Amplitude Perturbations

The Bogoliubov equations [Eqs. (54) and (55)] discussed in Section 1 characterize the small-amplitude excitations in the presence of any particular condensate associated with a given wave function Ψ. For a small to medium vortex-free axisymmetric condensate with $Na/d_0 \lesssim 1$, the equations have been solved numerically to determine the low-lying normal mode frequencies of a vortex-free condensate (see Refs. 44,2 and Fig. 10). Subsequent studies then focused on the case of a condensate containing a vortex on the axis of an axisymmetric trap.[45] Remarkably, the associated quasiparticle spectrum for a stationary (nonrotating) condensate with a singly quantized vortex contained a mode with positive normalization, relative angular mo-

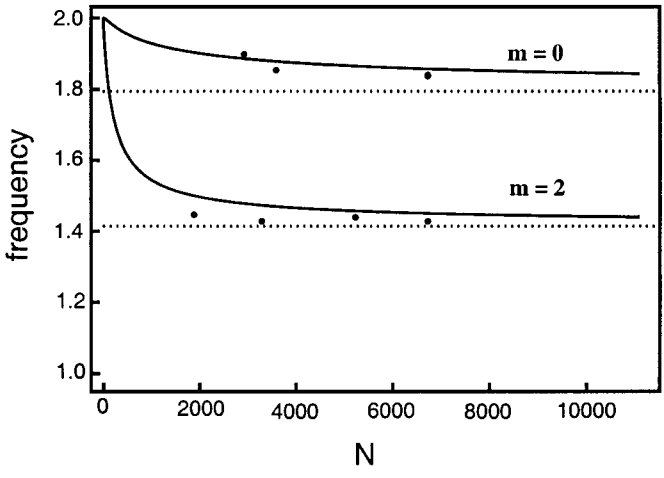

Fig. 10. Frequencies (in units of $\omega_\perp$) of the lowest collective modes of even parity for N rubidium atoms in the JILA trap. Dashed lines are the asymptotic TF results for $Na/d_\perp \to \infty$ (from Refs. 2,44).

mentum $m_a = -1$, and *negative* frequency ω_a. Such modes have become known as "anomalous" because of the sign of the frequency. The discussion associated with the quasiparticle Hamiltonian, Eq. (58), suggests that the condensate containing a vortex should be formally unstable because of the anomalous mode. In practice, some dissipative mechanism is needed for the instability to play a significant role, which is essentially the same point made in connection with curve (a) of Fig. 5. The GP equation has no intrinsic dissipation, and a vortex slightly displaced from the symmetry axis can only precess rather than spiral outwards and lose energy.

One can understand the mechanism associated with the anomalous mode by considering a nearly ideal Bose gas with a condensate containing a vortex. In this case, all the atoms are in the first excited harmonic-oscillator state with a wave function $\psi_1 \propto (x+iy)\exp(-\frac{1}{2}r_\perp^2/d_\perp^2) = r_\perp e^{i\phi}\exp(-\frac{1}{2}r_\perp^2/d_\perp^2)$ and unit angular momentum around the symmetry axis. This state has an energy $\hbar\omega_\perp$ higher than the true ground state with wave function $\psi_0 \propto \exp(-\frac{1}{2}r_\perp^2/d_\perp^2)$. In principle, each atom would prefer to make a transition back to the true ground state, with an energy change $-\hbar\omega_\perp$ and angular momentum change $m = -1$; this transition is just the anomalous mode in a noninteracting Bose gas; the interactions act to modify but not eliminate this mode. Indeed, numerical work for small and moderate condensates shows that the anomalous frequency $\omega_a = -|\omega_a|$ moves upward toward zero, but

even in the TF limit, the vortex state continues to have an anomalous mode whose frequency is given by[25]

$$\omega_a \approx -\frac{3}{2}\frac{\hbar}{MR_\perp^2}\ln\left(\frac{R_\perp}{\xi}\right). \tag{77}$$

As in the case of a uniformly moving condensate, it is instructive to consider the solutions of the Bogoliubov equations for a condensate in rotational equilibrium at an angular velocity Ω. Since the Hamiltonian is shifted by an amount $-\Omega L_z$, the eigenfrequencies of the Bogoliubov equations are also shifted from the original nonrotating values ω_j to

$$\omega_j(\Omega) = \omega_j - m_j\Omega, \tag{78}$$

where m_j is the angular momentum of the normal mode relative to that of the condensate. This expression shows how the eigenvalues shift with increasing Ω, analogous to Eq. (62) for a uniform translation.

For the anomalous mode with $m_a = -1$, the corresponding frequency in the rotating frame is

$$\omega_a(\Omega) = \omega_a + \Omega; \tag{79}$$

hence the applied rotation Ω shifts the negative anomalous frequency $-|\omega_a|$ *upward* toward zero. At a critical value Ω^* determined by $\omega_a(\Omega^*) = 0$, the anomalous mode ceases to be unstable, and the condensate with a vortex becomes stable with respect to these small-amplitude perturbations once $\Omega > \Omega^*$. In the present case of an axisymmetric condensate, Eq. (79) shows that this critical rotation frequency is simply

$$\Omega^* = -\omega_a = |\omega_a|, \tag{80}$$

namely the absolute value of the anomalous frequency. Comparison with Eq. (77) in the TF limit shows that $\Omega^* \approx \frac{3}{2}(\hbar/MR_\perp^2)\ln(R_\perp/\xi)$; this critical rotation frequency is identical with the metastability frequency Ω_m [Eq. (75)] defined in connection with Fig. 5.

The relevance of the quantum number m_j is clarified by considering the density perturbation associated with the jth Bogoliubov normal mode. It has the form $n_j' \propto \exp[i(m_j\phi - \omega_j t)]$, implying that the angular momentum quantum number m_j determines the angular dependence of the distortion. In particular, the density perturbation for the anomalous mode has a dipole character

$$n_a'(\phi, t) \propto e^{-i[\omega_a(\Omega)t+\phi]}, \tag{81}$$

which represents a small precessing displacement of the vortex core with an angular velocity $\dot{\phi} = -\omega_a(\Omega)$. For a nonrotating condensate with $\Omega = 0$ and

$\omega_a = -|\omega_a|$, the precession is in the *positive* sense, namely counterclockwise (this is in the same sense as the circulating flow around the vortex). Careful experiments at JILA[29] have indeed verified these predictions in great detail; for the experimental trap, the theory predicts $\dot{\phi}/2\pi \approx 1.58 \pm 0.16$ Hz and the measured value is 1.8 ± 0.1 Hz.

Note the crucial relation between the sense of the precession and the sign of the anomalous mode. The positive precession in a nonrotating condensate arises from the combined effect of the negative angular momentum quantum number $m_a = -1$ and the negative sign of ω_a. In a rotating condensate, the precession rate would appear slower and would eventually reverse for $\Omega > \Omega^*$, when the sign of the anomalous frequency becomes positive.

A vortex-free condensate has an infinite set of small-amplitude normal modes, and the low-lying ones have been studied in detail. The solutions are especially direct in the TF limit,[13] and low-temperature experiments[14,2] have confirmed the predicted frequency of the quadrupole modes with $l = 2$, $m = 0$ and $l = 2$, $m = \pm 2$ (see Fig. 10; these latter ones are degenerate and together they produce a quadrupole distortion). When the condensate has a vortex, however, its intrinsic sense of rotation affects these various normal modes, splitting the previously degenerate pairs with $\pm m$[46,47] (the effect is similar to the Zeeman splitting of the magnetic sublevels in the presence of an applied magnetic field, or the rotationally induced splitting of the earth's elastic normal modes). In the TF limit, the small fractional splitting is of order $|m|d_\perp^2/R_\perp^2$. For $l = 2$ and $|m| = 2$, the presence of the vortex means that the original quadrupole deformation slowly precesses because of the difference in the frequencies for $m = 2$ and $m = -2$.[32,48] Figure 11 shows some recent JILA pictures of a condensate with a quadrupole deformation. Figure 11 (a) has no vortex, and the deformation does not precess, whereas Figs. 11 (b) and (c) each show the predicted precessing deformation[48] [note that (b) and (c) refer to singly quantized vortices with opposite sense of circulation so that the precessions are in opposite directions]. This phenomenon serves as a clear signal for the presence of a vortex.

As noted by Zambelli and Stringari,[47] the magnitude of the splitting of the quadrupole mode can also provide a direct measure of the angular momentum of the condensate. This technique has been used in Paris (ENS) to detect when a vortex first appears in a rotating slightly nonaxisymmetric cigar-shaped condensate[32] and to verify that the angular momentum per particle is $\approx \hbar$.

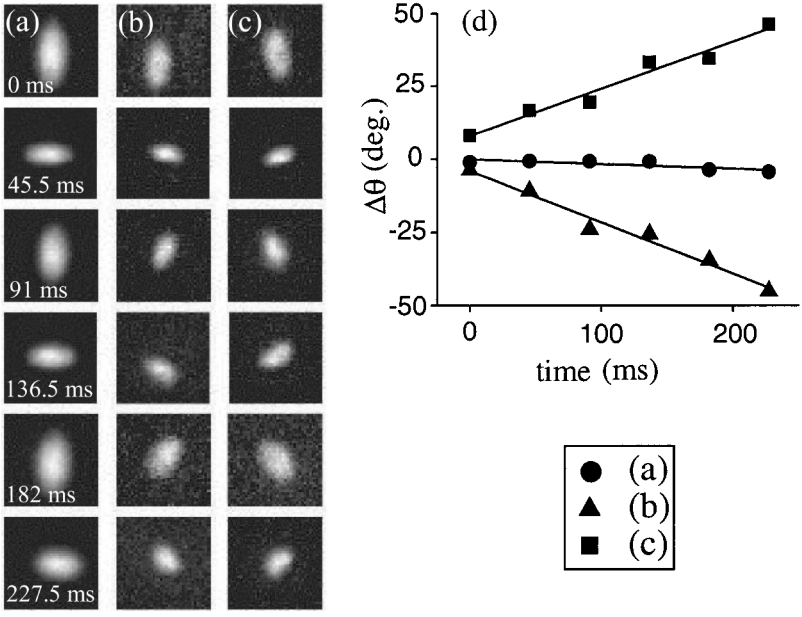

Fig. 11. Surface excitations provide an *in situ* detection of a vortex in a confined BEC. (a), (b), and (c) are each a series of nondestructive images of the quadrupole mode, after excitation. The pictures are strobed at 45.5 ms, half the excitation period. (a) is the case of a vortex-free condensate; (b) and (c) show the excitations in the presence of a vortex whose core is normal to the plane of the page. The vortices in (b) and (c) have opposite handedness. The principal axes of the ellipse-shaped quadrupole deformation precess in the direction of the fluid flow. The images are each fit to an elliptical distribution with an orientation angle $\Delta\theta$ of the principal axes. The orientation, expressed as an angular deviation from the horizontal and vertical axes, is plotted versus time in (d) for each of the cases (a), (b), and (c). A linear fit has been applied to the data to determine a precession frequency of the principal axes, -0.49(4) Hz for (b) and 0.45(5) Hz for (c). From Ref. 48.

2.5. Direct Analysis of Vortex Dynamics for a Rotating Anisotropic Condensate

At zero temperature, the dynamics of a condensate in a rotating nonaxisymmetric trap follows from the appropriate time-dependent GP equation

$$i\hbar\frac{\partial\Psi}{\partial t} = \left(-\frac{\hbar^2\nabla^2}{2M} + V_{\rm tr} + g|\Psi|^2 - \mu(\Omega) + i\hbar\mathbf{\Omega}\cdot(\mathbf{r}\times\boldsymbol{\nabla})\right)\Psi. \qquad (82)$$

A vortex line in the condensate will, in general, move in response to the effect of the nonuniform trap potential and the external rotation, as well as self-induced effects caused by its own local curvature. This problem can be solved in the case of a large condensate, where the TF separation of length scales means that the vortex-core radius ξ is much smaller than the condensate radii R_j. The relevant mathematics involves the method of matched asymptotic expansions.[49,50]

2.5.1. Dynamics of straight vortex in Thomas-Fermi regime for disk-shaped trap

As an introduction to these techniques, it is helpful first to concentrate on the case of a straight singly quantized vortex line,[28] which is applicable to disk-shaped condensates with $R_z \lesssim R_\perp$. Assume that the vortex is located near the center of the trap at a transverse position $\mathbf{r}_{\perp 0}(t)$. In this region, the trap potential does not change significantly on a length scale comparable with the vortex core size ξ. The method of matched asymptotic expansions compares the solution of Eq. (82) on two very different length scales.

First, consider the detailed structure of the vortex core. Assume that the vortex moves with a transverse velocity $\mathbf{V} \perp \hat{z}$, and transform to a co-moving frame centered at the vortex core. Away from the trap center, the trap potential exerts a force proportional to $\boldsymbol{\nabla}_\perp V_{\rm tr}$ evaluated at the position $\mathbf{r}_{\perp 0}(t)$. The resulting steady solution includes the "asymptotic" region $|\mathbf{r}_\perp - \mathbf{r}_{\perp 0}| \gg \xi$.

Second, consider the region far from the vortex (on this scale, the vortex core is effectively a singularity). The short-distance behavior of this latter solution also includes the region $\xi \ll |\mathbf{r}_\perp - \mathbf{r}_{\perp 0}|$. The requirement that the two solutions match in the overlapping region of validity determines the translational velocity $\mathbf{V}$ of the vortex line.

Unfortunately, the details become rather intricate, but the final answer is elegant and physical:

$$\mathbf{V} = \frac{3\hbar}{4M\mu}\left[\ln\left(\frac{R_\perp}{\xi}\right) - \frac{8\mu\Omega}{3\hbar\left(\omega_x^2+\omega_y^2\right)}\right](\hat{z}\times\boldsymbol{\nabla}_\perp V_{\rm tr})$$

$$= \frac{3\hbar}{4M\mu}\left[\ln\left(\frac{R_\perp}{\xi}\right) - \frac{2MR_\perp^2\Omega}{3\hbar}\right](\hat{z}\times\boldsymbol{\nabla}_\perp V_{\rm tr})\,, \tag{83}$$

where $R_\perp$ for an asymmetric trap is defined by $2/R_\perp^2 = 1/R_x^2 + 1/R_y^2$. This expression has several notable features.

- The motion is along the direction $\hat{z}\times\boldsymbol{\nabla}_\perp V_{\rm tr}$ and hence follows an equipotential line of $V_{\rm tr}$. Thus the trajectory conserves energy, which is expected because the GP equation omits dissipative processes. In the present case of an anisotropic harmonic trap, the trajectory is elliptical.

- For a nonrotating trap ($\Omega = 0$), the motion is counterclockwise in the positive sense at the frequency given by

$$\dot{\phi} = \frac{3}{2}\,\frac{\hbar}{MR_xR_y}\ln\left(\frac{R_\perp}{\xi}\right) \tag{84}$$

  proportional to $\omega_x\omega_y$. This expression generalizes the previous results for an axisymmetric condensate, where experiments confirm the correct sense of precession.[29]

- With increasing applied rotation Ω, the translational velocity $\mathbf{V}$ decreases and vanishes at the special value

$$\Omega_m = \frac{3\hbar\left(\omega_x^2+\omega_y^2\right)}{8\mu}\ln\left(\frac{R_\perp}{\xi}\right) = \frac{3\hbar}{2MR_\perp^2}\ln\left(\frac{R_\perp}{\xi}\right), \tag{85}$$

  proportional to $\frac{1}{2}\left(\omega_x^2+\omega_y^2\right)$. This value generalizes Eq. (75) associated with the onset of metastability for small transverse displacements of the vortex from center of an axisymmetric trap. For large asymmetry ω_y/ω_x, the metastable frequency Ω_m can significantly exceed the precession frequency $\dot{\phi}$ in a nonrotating trap.

- For $\Omega > \Omega_m$, the motion is clockwise as seen in the rotating frame. A detailed analysis based on the normalization of the Bogoliubov amplitudes shows that the positive-norm state has a frequency

$$\omega_a(\Omega) = \frac{2\omega_x\omega_y}{\omega_x^2+\omega_y^2}\left(\Omega - \Omega_m\right). \tag{86}$$

The normal-mode frequency is negative and hence unstable for $\Omega < \Omega_m$, but it becomes positive and hence stable for $\Omega > \Omega_m$; in this latter regime, the apparent sense of precession would be clockwise.

2.5.2. *Dynamics of curved vortex in Thomas-Fermi regime*

Consider a nonaxisymmetric trap that rotates with an angular velocity $\boldsymbol{\Omega}$ (for convenience, $\boldsymbol{\Omega}$ is often taken along the z axis). At low temperature in a frame rotating with the same angular velocity, the trap potential is time independent, and Eq. (82) describes the evolution of the condensate wave function. In the TF limit, the method of matched asymptotic expansions again yields an approximate solution for the motion of a singly quantized vortex line with instantaneous configuration $\mathbf{r}_0(z,t)$. Let $\hat{t}$ be the local tangent to the vortex (defined with the usual right-hand rule), $\hat{n}$ be the corresponding normal, and $\hat{b} \equiv \hat{t} \times \hat{n}$ be the binormal. A generalization of the previous approach eventually yields the explicit expression for the local translational velocity of the vortex[49]

$$\boldsymbol{V}(\boldsymbol{r}_0) = -\frac{\hbar}{2M}\left(\frac{\hat{t}\times\boldsymbol{\nabla}V_{\rm tr}(\boldsymbol{r}_0)}{g|\Psi_{\rm TF}|^2} + k\hat{b}\right)\ln\left(\xi\sqrt{\frac{1}{R_\perp^2}+\frac{k^2}{8}}\right) + \frac{2\,\boldsymbol{\nabla}V_{\rm tr}(\boldsymbol{r}_0)\times\boldsymbol{\Omega}}{\Delta_\perp V_{\rm tr}(\boldsymbol{r}_0)}, \tag{87}$$

where k is the local curvature (assumed small, with $k\xi \ll 1$) and $\Delta_\perp$ is the Laplacian operator in the plane perpendicular to $\boldsymbol{\Omega}$.

This vector expression holds for general orientations of the gradient of the trap potential, the normal to the vortex line, and the angular velocity vector. Near the TF boundary of the condensate, the denominator of the first term becomes small, implying that the numerator $\hat{t} \times \boldsymbol{\nabla} V_{\rm tr}(\mathbf{r}_0)$ must also vanish near the boundary. As a result, the axis of the vortex line $\hat{t}$ is parallel to $\boldsymbol{\nabla}V_{\rm tr}$ at the surface and hence obeys the intuitive boundary condition that the vortex must be perpendicular to the condensate surface.

Equation (87) allows a study of the dynamics of small-amplitude displacements of the vortex from the z axis, when $x(z,t)$ and $y(z,t)$ obey coupled equations. In the limit $\omega_z = 0$, there is no confinement in the z direction, and the density is independent of z. The resulting two-dimensional dynamics exhibits helical solutions that are linear combinations of two plane standing waves. They generalize the helical vortex waves that are familiar in superfluid ^{4}He[51] to include the effect of the transverse trap potential.

More generally, for $\omega_z \neq 0$, the density near the z axis has the TF parabolic form, and the solutions become more complicated. It is convenient to define the asymmetry parameters $\alpha = R_x^2/R_z^2$ and $\beta = R_y^2/R_z^2$, where $\alpha > 1$, $\beta > 1$ indicate a disk shape and $\alpha < 1$, $\beta < 1$ indicate a cigar shape.

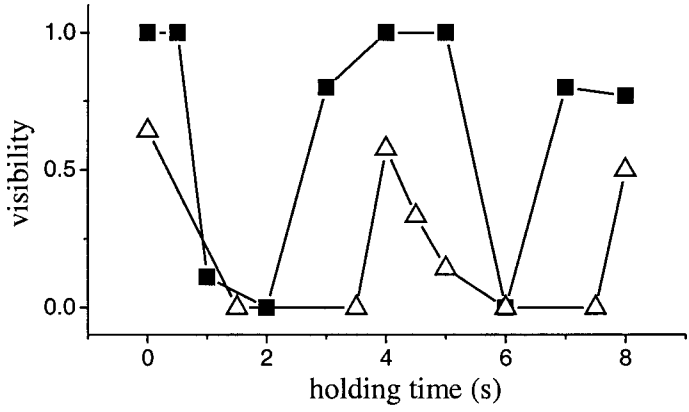

Fig. 12. Vortex visibility as the vortex precesses around an axis at 45° to the line of sight, plotted versus holding time in the trap. Filled squares indicate vortex detection with the surface-wave technique; open triangles indicate detection with the expansion technique (from Ref. 48).

- For a nonrotating trap with the special asymmetry values $\alpha = 2/[n(n+1)]$ (here, n is a positive integer), the effects of the nonuniform trap potential and the curvature just balance, and the condensate has stationary solutions with the vortex at rest in the xz plane. A disk-shaped trap has no such states, and the first one occurs for the spherical trap with $\alpha = 1$. The next such state occurs for $\alpha = \frac{1}{3}$, when the condensate is significantly elongated. Similar considerations for β apply to stationary states in the yz plane.

- For other values of α and β, solutions necessarily involve motion of the vortex line relative to the stationary condensate.

- Analytical solutions can be found for a flat disk with $\alpha \gg 1$ and $\beta \gg 1$, reproducing the frequency Ω_m found in Eq. (75) for an axisymmetric disk-shaped trap.

- For small deformations of a vortex line in an axisymmetric trap with $\alpha = \beta$, a disk-shaped or spherical condensate ($\alpha \geq 1$) has only a single (unstable) precessing normal mode with a negative frequency $\omega_a < 0$. In this case, an external rotation $\Omega \geq \Omega_m = |\omega_a|$ stabilizes the vortex. For these geometries, Ω_m is less than the thermodynamic critical value Ω_c. In a spherical condensate, the one anomalous mode $|\omega_a|$ agrees with the observed vortex precession frequency seen in the JILA experiments.[29,30]

- In contrast, an axisymmetric cigar-shaped condensate has additional negative-frequency precessing modes, and Ω_m can exceed Ω_c for sufficiently elongated condensates (this is very different from a disk-shaped TF condensate where $\Omega_m \approx \frac{3}{5}\Omega_c$). In the range $\Omega_c < \Omega < \Omega_m$, a bent vortex is the lowest-energy configuration, because a straight vortex undergoes a deformational instability.

- For a nearly spherical trap, Eq. (87) predicts that a straight vortex line through the center can execute *large-amplitude* periodic tilting trajectories. In this case, the vortex line becomes invisible when it tips away from the line of sight, and it then returns periodically to full visibility. Such revivals agree with observations at JILA,[48] where two recurrences have been seen. The experimental method uses two different techniques (see Fig. 12). The open triangles measure the visibility when the trap is turned off and the subsequent expansion detects the vortex through its expanded core; the black squares detect the vortex through the induced precession of the small-amplitude quadrupole deformation. As can be seen, both methods yield the same tilting frequency $\omega/2\pi \approx 0.25$ Hz, whereas the theory predicts a tilting frequency $\omega/2\pi \lesssim 0.3$ Hz (the experimental paper says "uncertainties in confinement asymmetry preclude more precise determination"), in reasonable agreement with the experimental value. For a totally asymmetric trap with $\omega_x < \omega_y < \omega_z$, the trajectories of the nearly straight vortex obey equations analogous to the Euler equations for the angular velocity as seen in the body-fixed frame for torque-free rigid-body motion. A vortex line oriented near $\hat{x}$ or $\hat{z}$ executes stable small-amplitude motion, whereas a vortex oriented near $\hat{y}$ executes large-amplitude but periodic orbits (see Ref. 49).

3. MIXTURES AND SPINOR CONDENSATES

One of the most interesting recent developments in Bose-Einstein condensates has been the possibility of confining simultaneously two distinct Bose species in the same trap.[52] This new experimental system has allowed a series of remarkable studies of coherence and indeed led to the first experimental creation of a vortex line.

3.1. Mixtures of Uniform Bose Condensates

The relative interactions between the two species play a crucial role. To understand the essential physics, it is simplest to consider a box of volume V containing a uniform Bose gas at zero temperature with N particles of each species 1 and 2.[53] The interparticle potentials are taken as short range, with

$$V_{ij}(\mathbf{r}-\mathbf{r}') \approx g_{ij}\,\delta(\mathbf{r}-\mathbf{r}'), \tag{88}$$

where i and $j = 1, 2$ denote the two different species. Assume that g_{ii} is positive, so that the self interactions are repulsive. Furthermore, symmetry requires that $g_{12} = g_{21}$. For the self-interaction parameters, we have $g_{ii} \approx 4\pi\hbar^2 a_{ii}/M_i$, where a_{ii} is the usual s-wave scattering length for the ith species. For the mutual interaction parameter, we have $g_{ij} \approx 2\pi\hbar^2 a_{ij}/M_{\rm red}$, where $1/M_{\rm red} = 1/M_1 + 1/M_2$ defines the usual reduced mass.

Suppose that the two species mix and overlap, so that each fills the whole volume V. The interaction energy arises from both species through their self interactions and their mutual interaction

$$E_{\rm mix} = \frac{N^2}{2V}\,(g_{11} + 2g_{12} + g_{22})\,. \tag{89}$$

If, instead, they do not mix and overlap, let V_1 and V_2 be the volumes that the two species occupy, with $V_1 + V_2 = V$. The interaction energy for this separated case is the sum of the two separate self-interaction energies

$$E_{\rm sep} = E_1 + E_2 = \frac{N^2}{2V_1}\,g_{11} + \frac{N^2}{2V_2}\,g_{22}. \tag{90}$$

The pressure in each region follows from the thermodynamic relation

$$p_i = -\frac{\partial E_i}{\partial V_i} = \frac{N^2}{2V_i^2}\,g_{ii}. \tag{91}$$

Mechanical equilibrium between the two regions requires that the pressures be equal, so that $g_{11}/V_1^2 = g_{22}/V_2^2$. It is easy to see that these relations imply

$$\frac{V}{V_1} = 1 + \sqrt{\frac{g_{22}}{g_{11}}} \quad \text{and} \quad \frac{V}{V_2} = 1 + \sqrt{\frac{g_{11}}{g_{22}}}, \tag{92}$$

so that the energy of the separated configuration is

$$E_{\rm sep} = \frac{N^2}{2V}\,(g_{11} + 2\sqrt{g_{11}g_{22}} + g_2)\,. \tag{93}$$

Comparison of Eqs. (89) and (93) show that $E_{\rm sep}$ is less than $E_{\rm mix}$ if

$$\sqrt{g_{11}g_{22}} < g_{12}, \tag{94}$$

which is the criterion for phase separation in a uniform system. If $g_{11}g_{22} < g_{12}^2$, the components are immiscible and the two species will separate into two phases, whereas if $g_{11}g_{22} > g_{12}^2$, the mixture is miscible and the two bulk species will mix. In the context of Bose gases, this criterion was first found through the appearance of imaginary frequencies in the Bogoliubov equations for a dilute mixture;[54] this instability of the uniform system indicates the onset of phase separation.

3.2. Mixtures of Bose Condensates in Harmonic Traps

The first theoretical attempt to include the presence of a trap relied on the TF description and imagined a mixture of distinct atoms with different scattering lengths,[55] for example $a \approx 2.75$ nm for ^{23}Na and $a \approx 5.77$ nm for ^{87}Rb. In practice, the interspecies scattering lengths are not known, and such an experiment has not been performed.

3.2.1. Boundary-layer corrections to Thomas-Fermi approximation

The use of the TF approximation can lead to considerable inaccuracies, and it is valuable to review briefly the leading corrections to the TF description[56] for a single component in an isotropic harmonic trap. We start from the GP equation that describes the isotropic condensate wave function $\Psi(r)$

$$\left(-\frac{\hbar^2\nabla^2}{2M} + \frac{M\omega^2 r^2}{2} + g|\Psi|^2\right)\Psi = \mu\Psi, \tag{95}$$

where the condensate density $|\Psi|^2$ varies on the scale of the condensate radius R. Thus the Laplacian ∇^2 scales like $1/R^2$ but the harmonic trapping potential scales like R^2. On this basis, the TF approximation neglects the kinetic energy entirely and finds the approximate parabolic density profile

$$|\Psi_{\rm TF}(r)|^2 \approx \frac{\mu}{g}\left(1 - \frac{r^2}{R^2}\right), \tag{96}$$

where $R = \sqrt{2\mu/M\omega^2}$. As discussed in Section 1, the TF approximation generally works well for large $Na/d_0 \gg 1$, where $d_0 = \sqrt{\hbar/M\omega}$ is the oscillator length. Near the surface of the condensate, however, it implies that

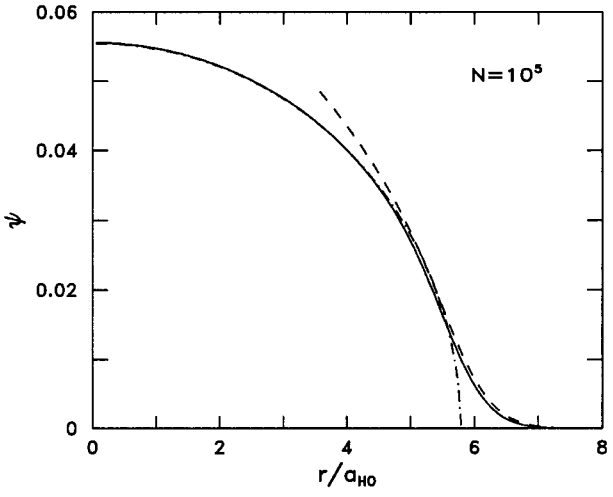

Fig. 13. Condensate wave function for 10^5 atoms of ^{87}Rb in a spherical harmonic trap of oscillator length 1.22 μm. Solid line: numerical solution of the GP equation. Dot-dashed line: Thomas-Fermi approximation (indistinguishable from the solid line in the inner part). Dashed line: surface profile obtained from boundary-layer approximation (from Ref. 56).

$\Psi_{\rm TF} \approx \sqrt{1 - r^2/R^2}$, which has an infinite derivative as $r \to R$. As a result, the TF kinetic energy $\langle T \rangle_{\rm TF} = (\hbar^2/2M) \int dV \, |\nabla \Psi_{\rm TF}|^2$ diverges logarithmically near the condensate surface. Consequently, the TF approximation cannot describe the small tail of the true condensate wave function for $r \gtrsim R$.

In fact, the GP equation leads to a thin boundary layer of thickness $\delta \ll R$ in the vicinity of the surface $r \approx R$. To understand the physics, it is convenient to introduce a scaled radial variable, writing $r = R + \delta x$, where x vanishes at the TF surface. In terms of x, the GP equation becomes

$$\left[-\frac{\hbar^2}{2M\delta^2} \nabla_x^2 + \frac{M\omega^2}{2} \left(2R\delta x + \delta^2 x^2 \right) + g|\Psi|^2 \right] \Psi = 0. \tag{97}$$

The boundary-layer thickness is chosen to balance the first two terms, so that $\delta^3 = \hbar^2/2M^2\omega^2 R = d_0^4/2R$; note that $\delta \ll d_0 \ll R$ in the TF limit. In the boundary layer $|x| \lesssim 1$, the condensate wave function is small and can be rescaled according to $\Psi(r) \propto \delta^{1/2} \Phi(x)$. This function $\Phi(x)$ matches the TF solution for $x \to -\infty$ (namely, deep in the condensate) and it vanishes exponentially for $x \to \infty$. It provides an accurate description of the small tail of the true wave function beyond the TF radius (see Fig. 13).

3.2.2. *Coupled Gross-Pitaevskii equations*

It is easy to study a pair of coupled GP equations for two condensate wave functions ψ_1 and ψ_2 describing the two components. It is convenient to choose the normalization $\int dV\,|\psi_i|^2 = 1$ for $i = 1, 2$, in which case we have

$$\left(T_1 + V_1 + N_1 g_{11}|\psi_1|^2 + N_2 g_{12}|\psi_2|^2\right)\psi_1 = \mu_1 \psi_1, \tag{98}$$

$$\left(T_2 + V_2 + N_1 g_{21}|\psi_1|^2 + N_2 g_{22}|\psi_2|^2\right)\psi_2 = \mu_2 \psi_2. \tag{99}$$

Here, T_i, V_i, N_i, and μ_i are the kinetic energy, the external trap potential, the total number, and the chemical potential for component i. The coupling occurs through the effective Hartree potentials

$$V_{H1} = N_1 g_{11}|\psi_1|^2 + N_2 g_{12}|\psi_2|^2 \quad \text{and} \quad V_{H2} = N_1 g_{21}|\psi_1|^2 + N_2 g_{22}|\psi_2|^2 \tag{100}$$

that are linear in the densities of the two components. In contrast to the uniform model considered previously, the spatial variation of the condensate wave functions leads to interesting questions involving the overlap of the two components. The TF approximation cannot handle these questions accurately, and numerical methods are usually used to solve these coupled GP equations.

3.2.3. *First experimental realization of coupled Bose condensates*

The coupled GP equations [Eqs. (98) and (99)] have many parameters, not all of which are known in most cases. For numerical simulations, it is usually preferable to simulate real experiments instead of studying a fictitious mixture of (say) ^{23}Na and ^{87}Rb that has not been realized in the laboratory. Thus we focus on the first experiment on boson mixtures,[52] which used two particular hyperfine states of ^{87}Rb.

As a brief review, this isotope has a nuclear spin $I = \frac{3}{2}$. It combines with the single valence electron ($S = \frac{1}{2}$) to form two hyperfine manifolds, a lower one with $F = 1$ and an upper one with $F = 2$. Because the trap has a local minimum in the magnetic field, only some of the hyperfine states are weak-field seeking and hence stable. In the notation $|F, m_F\rangle$, the stable ones are $|1, -1\rangle$, $|2, 1\rangle$, and $|2, 2\rangle$ (the remaining ones either have neutral stability with $m_F = 0$ or are unstable).

The experiment in question[52] used the specific components $|1, -1\rangle$ and $|2, 2\rangle$. They first made separate pure condensates of each component and studied them in detail, confirming the expected behavior. They then made

a mixture of the two components above the transition to Bose-Einstein condensation. Evaporative cooling was used to cool the species $|1,-1\rangle$, but the $|2,2\rangle$ component cooled only through "sympathetic cooling," which relies on thermal contact between the two components. This sympathetic cooling had previously been used for ions at much higher temperature, but this was the first application to neutral atoms.

Unfortunately, the details were somewhat intricate.

- The magnetic moment of the state $|2,2\rangle$ is twice that of the state $|1,-1\rangle$.
- As a result, the trapping frequency for $|2,2\rangle$ is more confining, with trap frequencies larger by a factor $\sqrt{2}$.
- These distinct trapping potentials mean that it is necessary to include the effect of gravity, which induces more displacement for the $|1,-1\rangle$ component because of the weaker confinement.

Careful numerical studies[57] included all these effects. They found a reasonable fit to the observations, which showed the $|2,2\rangle$ on top of the $|1,-1\rangle$ component because of gravity and the different confining potentials (see Fig. 14). The analysis used the following scattering lengths

$$a_{11} = 5.757 \text{ nm}, \quad a_{12} = 5.715 \text{ nm}, \quad a_{22} = 5.773 \text{ nm},$$

which fit the measured spin-exchange decay rate. Note that $a_{12}^2 < a_{11}a_{22}$, so that the condensates would mix if they were uniform; the physical separation arises from the trap and from the kinetic energy associated with the spatial variation of the two densities.

They also studied the spatial overlap of the two condensates by considering the quantity $\int dV\, |\psi_1|^2|\psi_2|^2$, which was much smaller than $\int dV\, |\psi_1|^4$ or $\int dV\, |\psi_2|^4$. The numerically determined theoretical wave functions yielded a lifetime of 6 s for each condensate assuming spin-exchange scattering is the only loss mechanism. In contrast, the TF approximation greatly underestimates the overlap and predicts a much longer lifetime (450 s). In fact, spin-exchange scattering competes with other loss mechanisms, such as dipolar relaxation (which is the dominant two-body loss process for like atoms) and three-body recombination. The theoretical analysis studied the dipolar relaxation as a function of the value of the interspecies interaction a_{12}; for the actual value, dipolar relaxation dominates for $|2,2\rangle$ and spin exchange dominates for $|1,-1\rangle$.

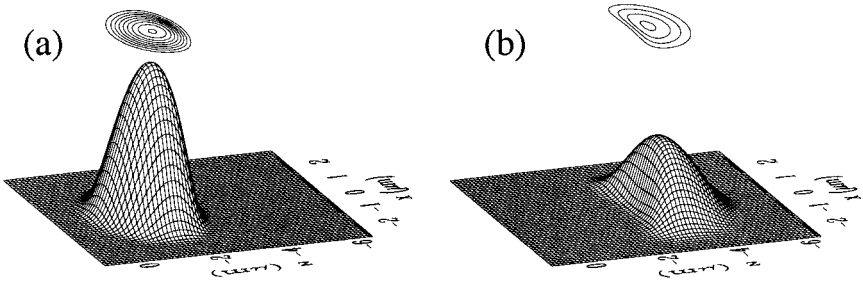

Fig. 14. Single-particle densities $|\psi_i(\mathbf{r})|^2$ in the plane $y = 0$: (a) $|2,2\rangle$ and (b) $|1,-1\rangle$, shown separately for clarity. Note that the z axis increases from right to left. The $|2,2\rangle$ state is more tightly confined and therefore closer to the nominal trap center $z = 0$ (from Ref. 57).

3.3. Physics of Interacting Condensates with Externally Applied Electromagnetic Coupling

In the second (and all subsequent) series of experiments, the JILA group used a different pair of hyperfine states:[58] $|1,-1\rangle \equiv |1\rangle$ and $|2,1\rangle \equiv |2\rangle$. This choice offers several advantages.

- The magnetic moments are essentially the same for both components, so that they experience the same trapping potentials.
- Each component is relatively long-lived because of an accidental coincidence between the singlet and triplet scattering lengths of ^{87}Rb.
- They can conveniently and quickly change atoms from $|1\rangle$ to $|2\rangle$ and back by a two-photon transition (microwave at 6.8 GHz plus rf at ≈ 2 MHz, see Fig. 15a).
- They can selectively image either component by using appropriately tuned lasers.

Subsequent experiments[23,29] showed that the $|2\rangle$ component is less stable because it can undergo spin-exchange scattering that changes the m_F values. In contrast to the state $|1\rangle$, the state $|2\rangle$ is not maximally aligned, so that the process $|2,1\rangle + |2,1\rangle \rightarrow |2,2\rangle + |2,0\rangle$ is allowed, producing the untrapped state $|2,0\rangle$.

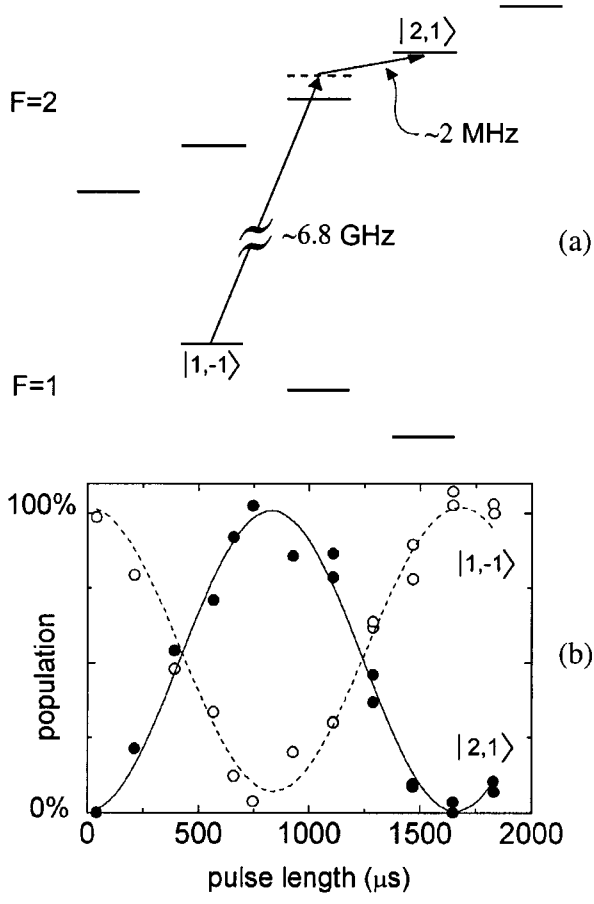

Fig. 15. (a) Diagram of the ground-state hyperfine levels ($F = 1, 2$) of ^{87}Rb shown with Zeeman splitting due to the presence of an applied magnetic field. The two-photon transition is driven between the $|1, -1\rangle$ and $|2, 2\rangle$ states. (b) The Rabi oscillation of population between the $|1, -1\rangle$ (open circles) and $|2, 2\rangle$ (solid circles) as a function of the two-photon drive duration. The lines are fit to the data and show the expected sinusoidal oscillation (from Ref. 58).

3.3.1. *Sudden transformation from* $|1\rangle$ *to* $|2\rangle$

A condensate with $\approx 5 \times 10^5$ atoms in state $|1\rangle$ is cooled below $0.4\,T_{\rm BEC}$, so that more than 75% of the atoms are in the condensate.[58] A short two-photon pulse then transfers essentially all the atoms to the $|2\rangle$ state. After a variable time delay, the trap was turned off, allowing the condensate to expand. Initially, the condensate shrank, followed by compressional oscillations. This behavior can be understood because $a_{11} > a_{22}$, so that the initial density profile following the transformation $|1\rangle \to |2\rangle$ no longer could sustain its radius and experienced shrinkage and radial oscillations. The behavior was modeled with a time-dependent GP equation

$$i\hbar\frac{\partial\Psi}{\partial t} = \left[-\frac{\hbar^2\nabla^2}{2M} + V_{\rm tr} + \frac{4\pi\hbar^2 a(t)}{M}|\Psi|^2\right]\Psi, \tag{101}$$

with $a(t)$ changing from a_{11} to a_{22} discontinuously at $t = 0$. A fit to the observations indicated that $a_{11}/a_{22} \approx 1.06$.

3.3.2. *Effect of applied electromagnetic field*

When the electromagnetic coupling is turned off, the two distinct condensates interact only through their Hartree (mean-field) potentials V_{H1} and V_{H2} that are linear in the density of the two components [see Eq. (100)]. In this case, each condensate is described by condensate wave functions Ψ_1 and Ψ_2 that are complex one-component order parameters. Each one has the representation $\Psi_j(\mathbf{r}) = |\Psi_j(\mathbf{r})|\exp[iS_j(\mathbf{r})]$. The wave function must be single-valued when $\mathbf{r}$ executes a closed path at any instant of time, so that the phase is 2π-periodic for any closed path. When this crucial observation that the phase must change by an integral multiple of 2π is combined with the result that $\mathbf{v}(\mathbf{r}) = (\hbar/M)\nabla S(\mathbf{r})$, it shows that the circulation $\oint_C d\mathbf{l}\cdot\mathbf{v}$ is quantized in units of h/M. This effect is well known in superfluid ^{4}He and in conventional BCS superconductors, where it leads to the quantization of magnetic flux.

A complex one-component order parameter displays $U(1)$ symmetry, which means that the order parameter is a complex scalar function. Apart from the magnitude $|\Psi|$ that is fixed by the temperature in a uniform system, such a one-component order parameter has only the phase that varies between 0 and 2π. This topology is that of a circle and yields quantized vorticity to ensure that the order parameter is single-valued. For $T \ll T_{\rm BEC}$, the magnitude of the bulk order parameter $|\Psi|$ is "large" and fluctuations are very improbable, which "explains" the persistent currents in superfluids and superconductors. The quantized circulation reflects the topological

charge of the enclosed state (the integer associated with the 2π periodicity of the phase of the order parameter). This charge is the winding number (think of a rubber band wrapped one or more times around a cylinder).

The situation is very different when the electromagnetic coupling is *turned on.* The coupling is now intrinsic and the resulting order parameter has two components, qualitatively changing its character. Any coupled two-component system can be thought of as analogous to a spin $\frac{1}{2}$;[59] the order parameter now has $SU(2)$ symmetry. The dynamics of the coupled system becomes similar to that of nuclear magnetic resonance, obeying what are called "optical Bloch equations." In the present case, the transformation of $|1\rangle$ into $|2\rangle$ is analogous to a π pulse that rotates a spin from up to down. If the pulse is twice as long, the resulting 2π rotation reproduces the initial $|1\rangle$ state. Experiments[58] verify the periodic transfer between the two populations as the length of the applied pulse varies (see Fig. 15b).

3.3.3. Dynamics of coupled interacting condensates

The simplest experiment transfers 50% from $|1\rangle$ to $|2\rangle$ with a $\pi/2$ pulse and then studies the behavior of the two interacting but separate condensates. The three scattering lengths obey the relation $a_{11} : a_{12} : a_{22} = 1.03 : 1.00 : 0.97$, with an average $a \approx 5.5$ nm. These values are right at the boundary for onset of phase separation in a uniform system. In a trap, one expects and finds a shell structure, with less repulsive $|2\rangle$ on the inside, allowing the more strongly repulsive $|1\rangle$ to expand against the trap potential. Before the pulse, the system is entirely $|1\rangle$; after the pulse, the initial condition is a 1:1 mixture but not in its equilibrium configuration. The near equality of the scattering lengths means that the total density remains nearly constant, but the two separate components execute highly damped normal-mode relative oscillations.[60] The final configuration has the centers separated largely because of the repulsive a_{12}. Nevertheless a significant overlap remains between the two components, allowing some very interesting experiments on the persistence of the relative phase.

To appreciate the crucial role of the electromagnetic coupling, it is helpful to write down the coupled GP equations for the two condensate wave functions[61]

$$i\hbar\frac{\partial}{\partial t}\begin{pmatrix}\psi_1\\ \psi_2\end{pmatrix} = \begin{pmatrix}T + V_1 + V_{H1} + \frac{1}{2}\hbar\delta & \frac{1}{2}\hbar\Omega(t)\\ \frac{1}{2}\hbar\Omega(t) & T + V_2 + V_{H2} - \frac{1}{2}\hbar\delta\end{pmatrix}\begin{pmatrix}\psi_1\\ \psi_2\end{pmatrix}, \quad (102)$$

where T is the kinetic energy, V_j is the trapping potential for component j, and V_{Hj} is the Hartree potential in Eq. (100) arising from both self and

mutual interactions. The applied microwave and rf field together lead to an effective "Rabi" frequency Ω that increases with the strength of the applied fields.[59] In general, this $\Omega(t)$ depends on t (for example, it vanishes when the applied coupling fields are turned off). Finally, δ is the detuning between the frequency of the driving field and that of the atomic hyperfine transition.

The experiment[61] starts with $\sim 5 \times 10^5$ atoms in the $|1\rangle$ state. At $t = 0$, a short $\pi/2$ pulse (400 μs) makes a second condensate $|2\rangle$ with approximately equal number of atoms $N_1 \approx N_2$. Each condensate then evolves by separating spatially, which takes ~ 50 ms; at this time, the two condensates still have a considerable spatial overlap. After a total time delay T, a second $\pi/2$ pulse is applied, and the trap is then turned off, allowing the system to expand so that it can be visualized.

After the first $\pi/2$ pulse, the two condensates have a definite relative phase ϕ_0. This relative phase then evolves at a rate proportional to the local difference in the chemical potentials of the two condensates ω_{12} as well as other contributions from the environment. In the overlap region, the effective relative phase after the time T is $\approx \delta T + \phi_0$, where $\delta = \omega_{12} - \omega_{\rm rf}$. The second $\pi/2$ pulse then remixes the two components. Depending on the accumulated phase difference, the density in the overlap region contains an interference term proportional to $\cos(\delta T + \phi_0)$. For example, the final density n_{2f} of state $|2\rangle$ is given by $n_{2f} \approx n_{1i} + n_{2i} + \sqrt{n_{1i}\, n_{2i}}\, \cos(\delta T + \phi_0)$, so that the overlap region can be in either the $|1\rangle$ or the $|2\rangle$ state because of constructive or destructive interference. The experiment sees many periods of such oscillations as T increases (see Fig. 16); the second trace shows that changing $\omega_{\rm rf}$ alters the period of the oscillation as expected from the $\cos(\delta T)$ dependence.

3.3.4. $U(1)$ vs. $SU(2)$ order parameters

A final pair of experiments highlight the essential difference between the $U(1)$ order parameter and the $SU(2)$ one. Each $U(1)$ order parameter is specified by a single complex number and its phase is like a unit vector confined to a plane oriented at the appropriate angle. In contrast, a coupled two-component system has an $SU(2)$ order parameter. In addition to the overall magnitude, this structure has *two* degrees of freedom associated with, for example, the angles in spherical polar coordinates; its topology is that of a sphere and does not require quantized vorticity. Thus the effective phase for the coupled system is like a unit vector that can point in any direction in three-dimensional space instead of being confined to a plane [which describes the $U(1)$ case]. The qualitative difference between the two

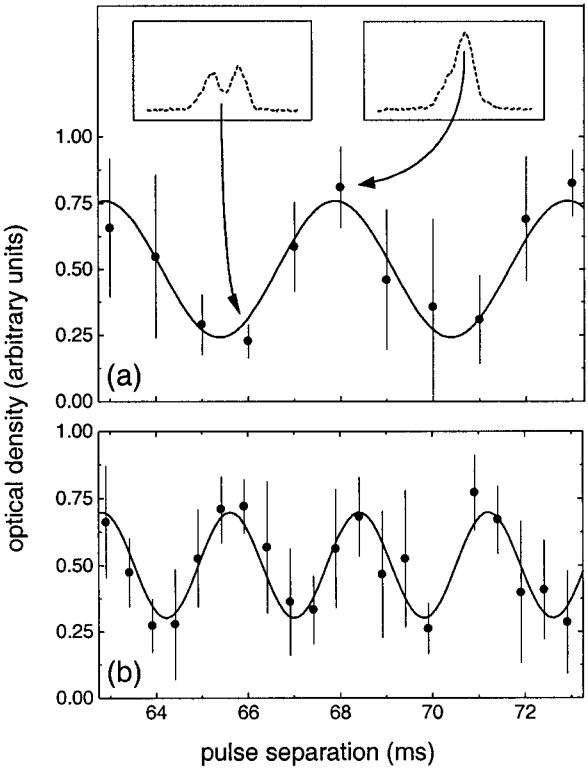

Fig. 16. The value of the condensate density in the $|2\rangle$ state is extracted at the center of the overlap region (inset) and plotted (a) as a function of T. Each point represents the average of six separate realizations, and the thin bars denote the rms scatter in the measured interference for an individual realization. The thick lines are sinusoidal fits to the data from which we extract the angular frequency $\omega_{21} - \omega_{\rm rf}$. In (b), the frequency of the coupling drive $\omega_{\rm rf}$ has been increased to $2\pi \times 150$ Hz, leading to the expected reduction in fringe spacing (from Ref. 61).

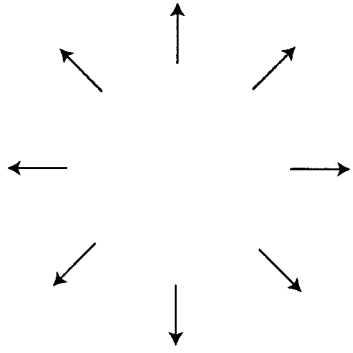

Fig. 17. Planar charge-1 vortex, with unit vectors pointing radially outward. In this form, the origin represents a singular point, and any closed path that encircles the origin finds a net increase of phase of 2π. If the unit vectors can rotate upward near the origin, however, the resulting three-dimensional structure is everywhere continuous and has no singularities.

cases can be understood as follows: the single degree of freedom of the one-component order parameter is like a rubber band wrapped around a cylinder, while the corresponding two degrees of freedom for the two-component order parameter is like a rubber band around the equator of a sphere. The former has a given winding number that can be removed only be cutting it (ensuring the quantization of circulation), whereas the latter can be removed simply by pulling it to one of the poles (so that there is no quantization).

As an instructive example, consider a planar charge-1 vortex in which the unit phase vectors point radially outward (see Fig. 17). Any closed path around the center finds an accumulated phase change of 2π. If this structure is instead considered in three dimensions, then the singularity at the center can be eliminated by rotating the vectors upward from horizontal to vertical near the center. In the study of liquid crystals, this latter behavior is called "escape into the third dimension." The point here is that each uncoupled condensate with $U(1)$ symmetry has quantized circulation associated with its own winding number. When the external electromagnetic coupling is turned on, however, the topology changes to that of a three-dimensional sphere, and the coupled system has new ways to minimize its total energy.

Such behavior was seen[62] by applying external fields with a spatial gradient, so that the precession of the $SU(2)$ order parameter varies with the spatial coordinate z. The increasing differential twist between the two ends relaxed periodically by a three-dimensional evolution of the effective phase (leading to collapses and recurrences, see Fig. 18). The theoretical basis for understanding this fascinating system has been developed in Ref. 63.

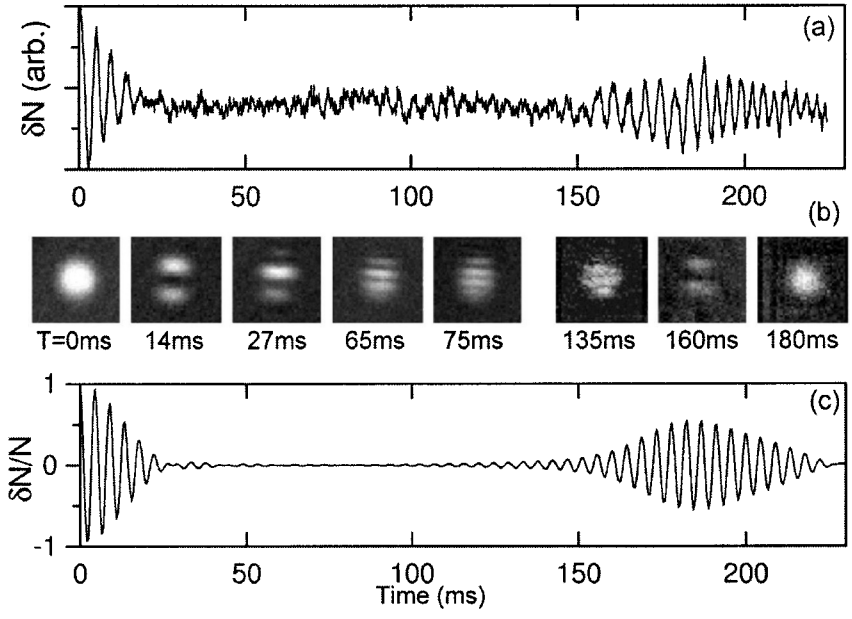

Fig. 18. A condensate with a large axial extent undergoes twisting. (a) The streak-camera data show a rapid decay in the Rabi oscillations in the integrated population difference, from full contrast at $t = 0$ to near zero contrast by $t = 20$ ms. The oscillations recur at 180 ms. (b) Individual phase-contrast images (at distinct moments in time) of the spatial distribution of $|1\rangle$-state atoms show that the spatially inhomogeneous Rabi frequency is twisting the order parameter, cranking successively more windings into the condensate until, by $\sim$ 75 ms, four distinct windings are visible. Further evolution results not in more but fewer windings until, at time 180 ms, the order parameter is once more uniform across the cloud. Each image block is 100 μm on a side, and the probe laser is tuned much closer to the $|1\rangle$ state than to the $|2\rangle$ state. (c) The numerical simulation reproduces the qualitative features of the corresponding experimental plot (a). From Ref. 62.

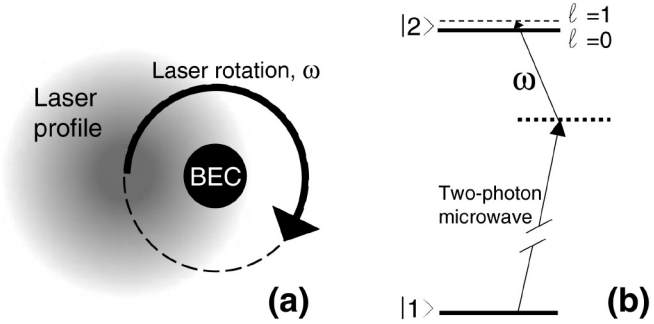

Fig. 19. (a) A basic schematic illustration of the technique used to create a vortex. An off-resonant laser provides a rotating force on the atoms across the condensate as a microwave drive of detuning δ is applied. (b) A level diagram showing the microwave transition to very near the $|2\rangle$ state, and the modulation due to the laser rotation frequency that couples only to the angular momentum $l = 1$ state when $\omega \approx \delta$ (from Ref. 23).

3.3.5. First creation of a vortex in a Bose-Einstein condensate

Williams and Holland[64] proposed adding an extra coupling arising from an external laser beam that displaces the trap centers for the two hyperfine states and rotates them at a frequency near the effective Rabi frequency of the applied electromagnetic fields (see Fig. 19). Starting from the ground state $|1\rangle$, this process creates the state $|2\rangle$ with one unit of angular momentum. Thus it constitutes a singly quantized vortex. They performed numerical simulation on a two-dimensional model, as shown in Fig. 20. The top graph shows the population of the $|2\rangle$ state as a function of time (the small-amplitude oscillations represent the cycling between the two different states caused by the off-resonance coupling). The bottom graph shows the corresponding angular momentum per particle. By turning off the coupling at an appropriate time, the $|2\rangle$ state is created with a vortex, and the circulation is now quantized because the order parameter has $U(1)$ symmetry after the coupling is removed.

This technique was used successfully to create the first vortex in a dilute trapped Bose condensate.[23] In this case, the vortex in the state $|2\rangle$ surrounds a nonrotating core of state $|1\rangle$. Since the state $|2\rangle$ has $m_F = 1$ (and therefore is not maximally aligned), it experiences spin relaxation with a lifetime of ~ 1 s. The process can start in either hyperfine state, so that it is easy to create a vortex in either state. The case of a vortex in $|1\rangle$ surrounding a core of $|2\rangle$ is more stable. Because of the spin relaxation, the core eventually decays leaving a more familiar one-component vortex. Section 2.3 discusses

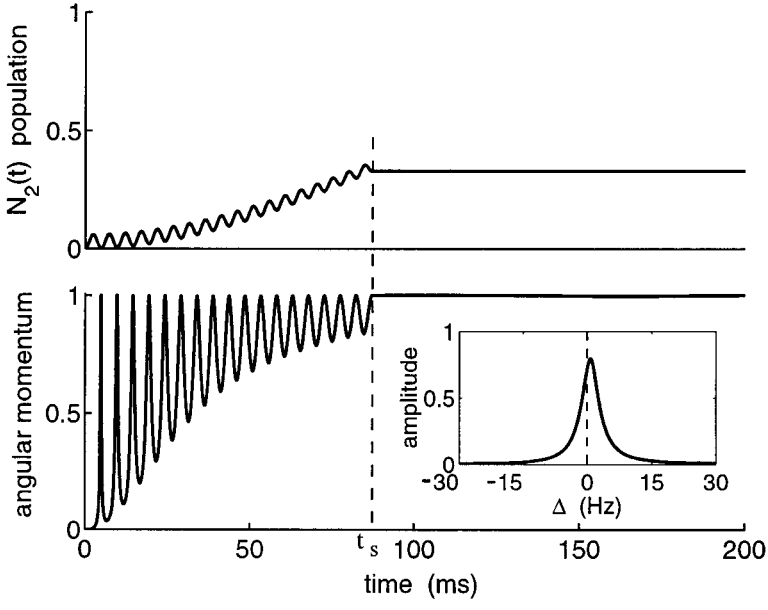

Fig. 20. Dynamical evolution to a vortex. These are results of numerical integration, with the condensate initially in the nonrotating ground state and in the internal state $|1\rangle$. The coupling drive is turned on at time $t = 0$ and is turned off at $t = t_s$. The top graph shows the fractional population of the atoms in the $|2\rangle$ internal state. The small-amplitude rapid oscillations correspond to the cycling between internal levels due to the off-resonant coupling. The gradual rise of this line is due to the coupling from the ground state to the vortex mode caused by the external drive. The bottom graph shows the angular momentum of the $|2\rangle$ state in units of $\hbar$. The rise and fall of this curve corresponds to a rapid cycling of the $|2\rangle$ atoms between the nonrotating condensate and the vortex. Once during each Rabi cycle, the angular momentum approaches unity, and at that time the $|2\rangle$ state wave function approaches a pure vortex mode. The inset shows the maximum amplitude of population transfer to the vortex as a function of the trap rotation frequency ω_r, with $\Delta = \Omega_{\rm eff} - \omega_r$ and $\Omega_{\rm eff}$ the effective Rabi frequency (from Ref. 64). Reprinted with permission from Nature copyright Macmillan Publishers Ltd.

some of the various experiments that have been performed.[29]

3.4. Spinor Bose-Einstein condensates in optical traps

In addition to the magnetic traps used in most studies of dilute trapped atomic gases, the MIT group has recently been able to trap ^{23}Na in a purely optical trap.[65] This new technique makes possible the creation of what is effectively a "spinor" condensate (for a recent review, see Ref. 53).

3.4.1. Optical traps

In an external electric field $\boldsymbol{\mathcal{E}}$, a polarizable object (such as an atom) acquires an electric dipole moment $\mathbf{p} = \alpha\boldsymbol{\mathcal{E}}$, where α is the atomic polarizability. The resulting energy is $U(\mathbf{r}) = -\frac{1}{2}\alpha|\mathcal{E}(\mathbf{r})|^2$. Equivalently, the polarizable object experiences a force $-\boldsymbol{\nabla}U(\mathbf{r})$ that attracts it to the region of large $|\mathcal{E}|^2$, assuming that α is positive (this is the case for an electrostatic field).

Suppose that the electric field oscillates at a frequency ω. The polarizability of an atom is given by a standard expression involving a sum of squared matrix elements of the dipole operator between the ground state and the various appropriate excited atomic states, divided by the corresponding energy denominators. For an alkali atom like ^{23}Na, the dominant transition is from nS to nP, ignoring the fine-structure splitting. To a very good approximation, the frequency-dependent polarizability of such an atom is given by

$$\alpha(\omega) \approx \frac{\text{const}}{\omega_{\text{PS}}^2 - \omega^2}, \tag{103}$$

where the numerator is positive and ω_{PS} is the frequency of the dominant transition (for ^{23}Na, these are the familiar yellow D lines). The most important conclusion here is that $\alpha > 0$ for red detuning with $\omega < \omega_{\text{PS}}$, but $\alpha < 0$ for blue detuning with $\omega > \omega_{\text{PS}}$. Thus a red detuned laser beam can trap atoms through pure dipole forces, independent of the hyperfine state. Conversely, a blue-detuned laser beam exerts a repulsive force on the atoms.

In the first experiment,[65] a conventional BEC was created with a magnetic trap and a red-detuned laser beam was then switched on. This laser beam traps the atoms and the magnetic trap can then be turned off. Like ^{87}Rb, the ^{23}Na atoms have a nuclear spin $\frac{3}{2}$, with the lowest hyperfine manifold being $F = 1$, containing the three sublevels $m_F = 1, 0, -1$. In contrast to the magnetic trap, all three of these sublevels are trapped by the red-detuned laser beam.

3.4.2. Spinor condensates: special case of spin-1

The possibility of trapping all three magnetic sublevels simultaneously rapidly led to the study of spin-1 Bose-Einstein condensates (as well as more general cases).[66] Unlike the previous mixtures of distinct species, we now have special restrictions arising from rotational invariance of the interactions between two spin-1 atoms. The macroscopic order parameter now becomes a spin-1 object with a three-component structure

$$\mathbf{\Psi} = \begin{pmatrix} \Psi_1 \\ \Psi_0 \\ \Psi_{-1} \end{pmatrix}. \tag{104}$$

In the low-energy limit where only s-wave scattering is relevant, the interaction between two atoms has the form

$$V_{\rm int}(\mathbf{r}_1 - \mathbf{r}_2) = \delta(\mathbf{r}_1 - \mathbf{r}_2) \sum_F \frac{4\pi\hbar^2 a_F}{M} \mathcal{P}_F, \tag{105}$$

where F is the magnitude of the total hyperfine spin $\mathbf{F} = \mathbf{F}_1 + \mathbf{F}_2$ and $\mathcal{P}_F$ is the projection operator onto the appropriate value of the total hyperfine spin.

For bosons with hyperfine spin 1, the only allowed values are $F = 0$ and $F = 2$, with two scattering lengths a_0 and a_2. The interaction potential can be written in the equivalent form

$$V_{\rm int}(\mathbf{r}_1 - \mathbf{r}_2) = \delta(\mathbf{r}_1 - \mathbf{r}_2) \left(g_0 + g_2 \mathbf{F}_1 \cdot \mathbf{F}_2\right), \tag{106}$$

where the effective interactions are given by

$$g_0 = \frac{4\pi\hbar^2}{M} \frac{2a_2 + a_0}{3}, \quad g_2 = \frac{4\pi\hbar^2}{M} \frac{a_2 - a_0}{3}. \tag{107}$$

To describe the equilibrium state of the spinor condensate, Ho[66] introduced an effective energy functional for the spinor order parameter written in the form $\Psi_\alpha(\mathbf{r}) = \sqrt{n(\mathbf{r})}\,\zeta_\alpha(\mathbf{r})$, where α runs over the values 1, 0, -1, $n(\mathbf{r})$ is the common density for all three components, and $\zeta_\alpha(\mathbf{r})$ is a normalized spinor with $\zeta^\dagger \cdot \zeta = 1$. The ground-state structure of Ψ_α follows by minimizing the energy with fixed total particle number (enforced through the chemical potential as a Lagrange multiplier). This procedure yields the effective energy functional

$$K = \int dV \left(\frac{\hbar^2}{2M} \left(\boldsymbol{\nabla}\sqrt{n}\right)^2 + \frac{\hbar^2}{2M} \left(\boldsymbol{\nabla}\zeta\right)^2 n - n\left[\mu - V_{\rm tr}(\boldsymbol{r})\right] + \frac{n^2}{2}\left(g_0 + g_2 \langle \boldsymbol{F} \rangle^2\right) \right). \tag{108}$$

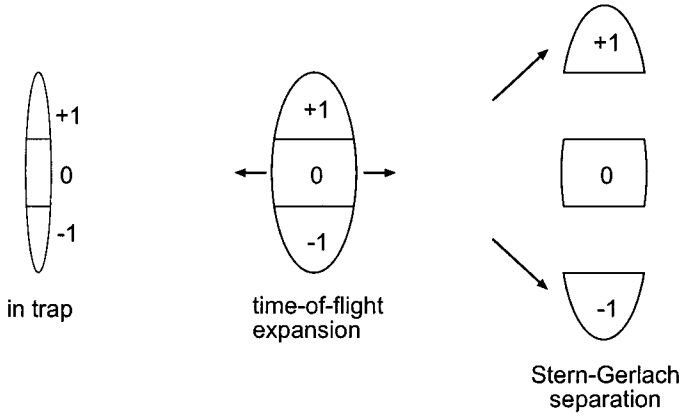

Fig. 21. Probing spinor condensates. After release from the elongated optical trap, the trapped spinor condensate expands primarily radially while maintaining the axial hyperfine distribution. A magnetic field gradient is then used to separate out the different components while preserving their shape. A subsequent absorption probe reveals the spatial and hyperfine distributions in the trap. From Ref. 53.

Here, the external trap potential is assumed to be independent of the hyperfine spin, and μ determines the total number of atoms in the trap.

Apart from the gradient terms, the ground-state spinor ζ_α is determined by minimizing the spin-dependent part of the energy $\frac{1}{2}n^2 g_2 \langle \mathbf{F} \rangle^2$, where $\langle \mathbf{F} \rangle = \sum_{\alpha\beta} \zeta_\alpha^* \mathbf{F}_{\alpha\beta} \zeta_\beta$ is the appropriate expectation value. There are two distinct solutions depending on the sign of the coupling constant g_2. If $g_2 > 0$, then the condensate lowers its energy by minimizing the average spin, namely $|\langle \mathbf{F} \rangle| = 0$. These states are called "polar" and they are those obtained by spatial rotations of the hyperfine state $|m_F = 0\rangle$. This situation applies to ^{23}Na. If $g_2 < 0$, then the condensate lowers its energy by maximizing the average spin, namely $|\langle \mathbf{F} \rangle| = 1$. These states are called "ferromagnetic" and they are those obtained by spatial rotations of the hyperfine state $|m_F = 1\rangle$. This situation apparently applies to ^{87}Rb.

Ketterle's group at MIT has performed an elegant series of experiments on this spinor condensate using ^{23}Na in an optical trap.

- Stenger *et al.*[67] studied the formation of spin domains in great detail. By carefully structuring the magnetic field, they could obtain various spin domains that were subsequently observed by a time-of-flight expansion followed by a Stern-Gerlach separation of the various spin components. The miscibility or immiscibility of the different compo-

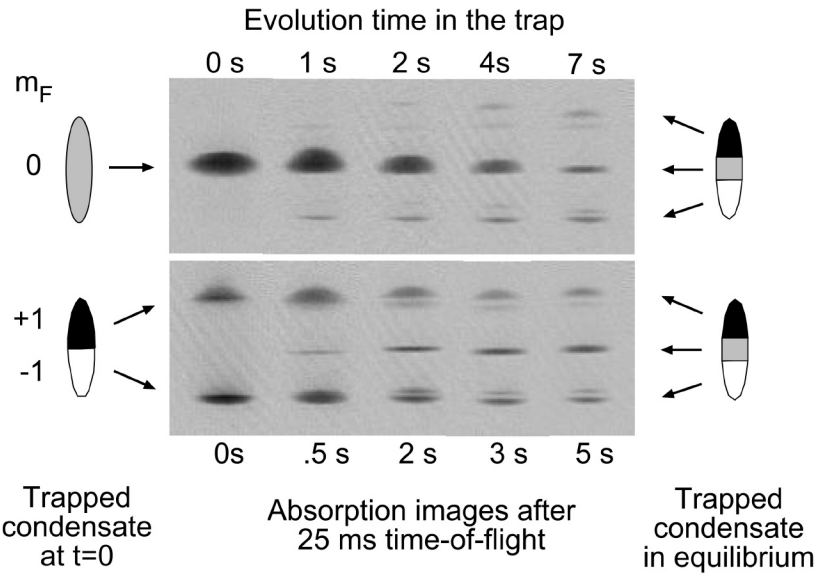

Fig. 22. Formation of the ground-state spin domains. Absorption images of ballistically expanding spinor condensates show both the spatial and hyperfine distributions. The images of clouds with various dwell times in the trap show the evolution to the same equilibrium for condensates prepared in either a pure $|m_F = 0\rangle$ state (upper row) or in equally populated $|m_F = \pm 1\rangle$ states (lower row). From Ref. 53.

nents follows from the previous considerations about mixtures. Figure 21 illustrates the technique (from Ref. 53).

- Miesner *et al.*[68] prepared long-lived metastable excited states (arising from the immiscibility of some of the various components). The time evolution occurs through quantum tunneling and through spin relaxation; Figure 22 shows some of the possible time-dependent behaviors.

- Stamper-Kurn *et al.*[69] carried out detailed studies of the quantum tunneling from the metastable to the final stable configurations. The tunneling rates provide a sensitive probe of the boundary between spin domains. They found a good fit to the Fowler-Nordheim (WKB) relation.

ACKNOWLEDGMENTS

Most of this material was originally produced as lecture notes for "Enseignement de 3ème cycle en Suisse Romande," June 2001. I am grateful to P.-A. Bares and Ph. Martin for their hospitality at the École Polytechnique Fédéral de Lausanne. I thank E. Cornell, F. Dalfovo, J. Dalibard, M. Edwards, B. Esry, M. Holland, and W. Ketterle for their permission for and assistance with the various figures. Part of the work reported here was supported by the National Science Foundation Grant No. DMR 9971518.

REFERENCES

1. *Bose-Einstein Condensation in Atomic Gases*, Proceedings of the International School of Physics "Enrico Fermi," edited by M. Inguscio, S. Stringari, and C. E. Wieman (IOP Press, Amsterdam, 1999).
2. F. Dalfovo, S. Giorgini, L. P. Pitaevskii, and S. Stringari, *Rev. Mod. Phys.* **71**, 463 (1999).
3. Y. Castin, in *Coherent Atomic Matter Waves*, Lecture notes of Les Houches Summer School, 1999, edited by R. Kaiser, C. Westbrook, and F. David (EDP Sciences and Springer-Verlag, 2001), pp. 1-136 (e-print:*cond-mat*/0105058).
4. E. M. Lifshitz and L. P. Pitaevskii, *Statistical Physics*, 3rd edition, Part 1 (Pergamon Press, Oxford, 1980), Chapter 5.
5. A. L. Fetter and J. D. Walecka, *Quantum Theory of Many Particle Systems* (McGraw-Hill, New York, 1971), Chapters. 1 and 2.
6. M. H. Anderson, J. R. Ensher, M. R. Matthews, C. E. Wieman, and E. A. Cornell, *Science* **269**, 198 (1995).
7. N. N. Bogoliubov, *J. Phys. (USSR)* **11**, 23 (1947).
8. See, for example, in Ref. 5, Section 35 and A.L. Fetter, in Ref. 1, p. 201.
9. E. P. Gross, *Nuovo Cimento* **20**, 454 (1961).
10. L. P. Pitaevskii, *Zh. Eksp. Teor. Fiz.* **40**, 646 (1961) [*Sov. Phys.–JETP* **13**, 451 (1961)].
11. L. D. Landau and E. M. Lifshitz, *Fluid Mechanics*, 2nd edition (Pergamon Press, London, 1987), Chapter I.
12. G. Baym and C. J. Pethick, *Phys. Rev. Lett.* **76**, 6 (1996).
13. S. Stringari, *Phys. Rev. Lett.* **77**, 2360 (1996).
14. D. M. Stamper-Kurn, H.-J. Miesner, S. Inouye, M. R. Andrews, and W. Ketterle, *Phys. Rev. Lett.* **81**, 500 (1998).
15. A. L. Fetter, *Ann. Phys. (N.Y.)* **70**, 67 (1972).
16. A. L. Fetter, *Phys. Rev. A* **53**, 4245 (1996).
17. C. C. Bradley, C. A. Sackett, and R. G. Hulet, *Phys. Rev. Lett.* **78**, 985 (1997).
18. S. L. Cornish, N. R. Claussen, J. L. Roberts, E. A. Cornell, and C. E. Wieman, *Phys. Rev. Lett.* **85**, 1795 (2000).
19. J. L. Roberts, N. R. Claussen, S. L. Cornish, E. A. Donley, E. A. Cornell, and C. E. Wieman, *Phys. Rev. Lett.* **86**, 4211 (2001).

20. E. A. Donley, N. R. Claussen, S. L. Cornish, J. L. Roberts, E. A. Cornell, and C. E. Wieman, *Nature* **412**, 295 (2001).
21. A. Robert, O. Sirjean, A. Browaeys, J. Poupard, S. Nowak, D. Boiron, C. I. Westbrook, and A. Aspect, *Science* **292**, 461 (2001).
22. F. Pereira Dos Santos, J. Léonard, J. Wang, C. J. Barrelet, F. Perales, E. Rasel, U. Unnikrishnan, M. Leduc, and C. Cohen-Tannoudji, *Phys. Rev. Lett.* **86**, 3459 (2001).
23. M. R. Matthews, B. P. Anderson, P. C. Haljan, D. S. Hall, C. E. Wieman, and E. A. Cornell, *Phys. Rev. Lett.* **83**, 2498 (1999).
24. K. W. Madison, F. Chevy, W. Wohlleben, and J. Dalibard, *Phys. Rev. Lett.* **84**, 806 (2000).
25. A. L. Fetter and A. A. Svidzinsky, *J. Phys. Cond. Matter* **13**, R135 (2001).
26. R. P. Feynman, in *Progress in Low Temperature Physics*, edited by C. J. Gorter (North-Holland, Amsterdam, 1955), Vol. 1, p. 17.
27. M. Tinkham, *Introduction to Superconductivity* (McGraw-Hill, New York, 1996), 2nd edition, Chapters. 4 and 5.
28. A. A. Svidzinsky and A. L. Fetter, *Phys. Rev. Lett.* **84**, 5919 (2000).
29. B. P. Anderson, P. C. Haljan, C. E. Wieman, and E. A. Cornell, *Phys. Rev. Lett.* **85**, 2857 (2000).
30. D. L. Feder, A. A. Svidzinsky, A. L. Fetter, and C. W. Clark, *Phys. Rev. Lett.* **86**, 564 (2001).
31. K. W. Madison, F. Chevy, W. Wohlleben, and J. Dalibard, *J. Mod. Opt.* **47**, 2715 (2000).
32. F. Chevy, K. W. Madison, and J. Dalibard, *Phys. Rev. Lett.* **85**, 2223 (2000).
33. F. Dalfovo and S. Stringari, *Phys. Rev. A* **63**, 011601(R) (2001).
34. S. Sinha and Y. Castin, *Phys. Rev. Lett.* **87**, 190402 (2001).
35. K. W. Madison, F. Chevy, V. Bretin, and J. Dalibard, *Phys. Rev. Lett.* **86**, 4443 (2001).
36. F. Chevy, K. W. Madison, V. Bretin, and J. Dalibard, in *Proceedings of Trapped Particles and Fundamental Physics Workshop (Les Houches 2001)*, edited by S. Atutov, K. Kalabrese, and L. Moi, e-print: *cond-mat*/0104218.
37. E. J. Yarmchuk, M. J. V. Gordon, and R. E. Packard, *Phys. Rev. Lett.* **43**, 214 (1979).
38. J. R. Abo-Shaeer, C. Raman, J. M. Vogels, and W. Ketterle, *Science* **292**, 476 (2001).
39. C. Raman, J. R. Abo-Shaeer, J. M. Vogels, K. Xu, and W. Ketterle, *Phys. Rev. Lett.* **87**, 210402 (2001).
40. P. C. Haljan, I. Coddington, P. Engels, and E. A. Cornell, *Phys. Rev. Lett.* **87**, 210403 (2001).
41. T.-L. Ho, *Phys. Rev. Lett.* **87**, 060403 (2001).
42. A. L. Fetter, *Phys. Rev. A* **64**, 063608 (2001).
43. U. R. Fischer and G. Baym, e-print: *cond-mat*/0111443, v.4.
44. M. Edwards, P. A. Ruprecht, K. Burnett, R. J. Dodd, and C. W. Clark, *Phys. Rev. Lett.* **77**, 1671 (1996).
45. R. J. Dodd, K. Burnett, M. Edwards, and C. W. Clark, *Phys. Rev. A* **56**, 587 (1997).
46. A. A. Svidzinsky and A. L. Fetter, *Phys. Rev. A* **58**, 3168 (1998).

47. F. Zambelli and S. Stringari, *Phys. Rev. Lett.* **81**, 1754 (1998).
48. P. C. Haljan, B. P. Anderson, I. Coddington, and E. A. Cornell, *Phys. Rev. Lett.* **86**, 2922 (2001).
49. A. A. Svidzinsky and A. L. Fetter, *Phys. Rev. A* **62**, 063617 (2000).
50. L. M. Pismen, *Vortices in Nonlinear Fields* (Clarendon Press, Oxford, 1999), Sections. 2.2 and 5.2.
51. R. J. Donnelly, *Quantized Vortices in Helium II* (Cambridge University Press, Cambridge, 1991), Chapter 6.
52. C. J. Myatt, E. A. Burt, R. W. Ghrist, E. A. Cornell, and C. E. Wieman, *Phys. Rev. Lett.* **78**, 586 (1997).
53. D. M. Stamper-Kurn and W. Ketterle, Les Houches 1999 Summer School, Session LXXII, e-print: *cond-mat*/0005001.
54. Y. A. Nepomnyashchii, *Teor. Mat. Phys.* **20**, 399 (1974).
55. T.-L. Ho and V. B. Shenoy, *Phys. Rev. Lett.* **77**, 3276 (1996).
56. F. Dalfovo, L. P. Pitaevskii, and S. Stringari, *Phys. Rev. A* **54**, 4213 (1996).
57. B. D. Esry, C. H. Greene, J. P. Burke, Jr., and J. L. Bohn, *Phys. Rev. Lett.* **78**, 3594 (1997).
58. M. R. Matthews, D. S. Hall, D. S. Jin, J. R. Ensher, C. E. Wieman, E. A. Cornell, F. Dalfovo, C. Minniti, and S. Stringari, *Phys. Rev. Lett.* **81**, 243 (1998).
59. See, for example, L. Allen and J. H. Eberly, *Optical Resonance and Two-Level Atoms* (Dover, New York, 1987), Chapters 2 and 3.
60. D. S. Hall, M. R. Matthews, J. R. Ensher, C. E. Wieman, and E. A. Cornell, *Phys. Rev. Lett.* **81**, 1539 (1998).
61. D. S. Hall, M. R. Matthews, C. E. Wieman, and E. A. Cornell, *Phys. Rev. Lett.* **81**, 1543 (1998).
62. M. R. Matthews, B. P. Anderson, P. C. Haljan, D. S. Hall, M. J. Holland, J. E. Williams, C. E. Wieman, and E. A. Cornell, *Phys. Rev. Lett.* **83**, 3358 (1999).
63. J. Williams, R. Walser, J. Cooper, E. A. Cornell, and M. Holland, *Phys. Rev. A* **61**, 033612 (2000).
64. J. E. Williams and M. J. Holland, *Nature* **401**, 568 (1999).
65. D. M. Stamper-Kurn, M. R. Andrews, A. P. Chikkatur, S. Inouye, H.-J. Miesner, J. Stenger, and W. Ketterle, *Phys. Rev. Lett.* **80**, 2027 (1998).
66. T.-L. Ho, *Phys. Rev. Lett.* **81**, 742 (1998).
67. J. Stenger, S. Inouye, D. M. Stamper-Kurn, H.-J. Miesner, A. P. Chikkatur, and W. Ketterle, *Nature* **396**, 345 (1998).
68. H.-J. Miesner, D. M. Stamper-Kurn, J. Stenger, S. Inouye, A. P. Chikkatur, and W. Ketterle, *Phys. Rev. Lett.* **82**, 2228 (1999).
69. D. M. Stamper-Kurn, H.-J. Miesner, A. P. Chikkatur, S. Inouye, J. Stenger, and W. Ketterle, *Phys. Rev. Lett.* **83**, 661 (1999).